MEASUREMENT AND MAGNITUDE-BASED SYSTEM IDENTIFICATION OF TORNADO-ASSOCIATED INFRASOUND

By

Brandon C. White

Bachelor of Science in Aerospace Engineering
Oklahoma State University
Stillwater, OK
2019

Bachelor of Science in Mechanical Engineering
Oklahoma State University
Stillwater, OK
2019

Submitted to the Faculty of the
Graduate College of
Oklahoma State University
in partial fulfillment of
the requirements for
the Degree of
MASTERS OF SCIENCE
July, 2021

MEASUREMENT AND MAGNITUDE-BASED SYSTEM IDENTIFICATION OF TORNADO-ASSOCIATED INFRASOUND

Thesis Approved:

Dr. Imraan Faruque - Thesis Advisor, Committee Head

Dr. Brian Elbing - Committee Member

Dr. He Bai - Committee Member

ACKNOWLEDGMENTS

I would like to thank all my friends and family who have helped to guide me to this point in my life through all of their continuous support, endless patience, and willingness to drag me away from work to keep me living life even when it seem like there are mountains of work still to do. Without you, I would not have been able to make it through the strife and struggle of a Master's degree program (especially during a pandemic).

I would additionally like to thank several of my fellow students at Oklahoma State University for their assistance in my work and for listening always so kindly as I ranted and raved: Ujjval Patel, Timothy Runnels, Katrine Harland, Chris Petrin, KC Real, and Trevor Wilson as well as the rest of the APG team

Finally, I would like to thank the members of the faculty of Oklahoma State University with which I worked for their contributions to this work. I would like to thank extend an additional thank you to Dr. Arena and Dr. Jacob for directing me into research and graduate school all the way back in the middle of undergrad.

I don't have the room on this page to properly thank everyone who deserves it, but from the heart, know that I am eternally grateful to each and every person who has helped me reach this point.

Acknowledgments reflect the views of the author and are not endorsed by committee members or Oklahoma State University.

Name: BRANDON C. WHITE

Date of Degree: July, 2021

Title of Study: MEASUREMENT AND MAGNITUDE-BASED SYSTEM IDENTIFICATION OF TORNADO-ASSOCIATED INFRASOUND

Major Field: MECHANICAL AND AEROSPACE ENGINEERING

Abstract: Recent evidence indicates that acoustic waves at frequencies below human hearing (infrasound) are produced during tornadogenesis and continue through the life of a tornado. The currently available tornadic infrasound data remains sparse, which has prevented the identification of the fluid mechanism responsible for its production. To increase the probability of detection, this thesis presents an adaptation of fixed infrasound sensing technology to equip storm chasers that are in regular proximity to tornadoes with mobile infrasound measurement capabilities. This approach has and continues to increase the quantity of samples while also reducing the long-range propagation-related uncertainties in the measurement analysis. This thesis describes the design and deployment of the Ground-based Local INfrasound Data Acquisition (GLINDA) system - a system which includes a specialized infrasound microphone, GPS receiver, and an IMU package for data remote collection. This thesis additionally presents analyses of measurements during an EFU tornado and a significant hail event as collected by the GLINDA system. The measured signal from the EFU tornado event notably produced an elevated broadband signal between 10 and 15 Hz consistent with past observations from small tornadoes. Frequency peak identification approaches are discussed in context of the EFU tornado. Utilizing the tornado event's frequency response magnitude as the output and a selection of wind noise pressure and energy models considered for acoustic response forcing inputs, frequency response system identification approaches are utilized to develop a set of transfer function models for the tornado acoustic production mechanism.

TABLE OF CONTENTS

LIST OF TABLES

LIST OF FIGURES

CHAPTER I

Introduction

1.1 Motivations

Tornadoes remain a significant hazard to life and property. In the United States, 800 -1400 annually reported tornadoes claim an average of 55 lives [4; 41] with 76 confirmed fatalities in the United States in 2020 [38]. Historical approaches to detecting and localizing tornadic structures have traditionally used radar as the driving measurement device for identifying areas of likely tornadogenesis. It then follows that many of these fatalities occur in the southeast United States due, in part, to hilly terrain limiting line-of-sight measurements such as radar.

These limitations have, in part, motivated a search for alternative methods to support and/or supplement radar measurements in hopes of improving tornado warnings. Infrasound, sound below human hearing (< 20 Hz), is one such possibility. Evidence from the last three decades of study indicates that infasonic acoustic waves are produced during tornadogenesis and continue through the life of a tornado, giving potential to locate and profile tornadic events even at distances up to on order of magnitude for modern radar detection capabilities. Specifically, infrasound in the nominal range of 0.5 to 10 Hz has been observed coming from the same region as tornadoes that were verified with Doppler radar and/or visual observations [7; 8; 16; 18; 24]. These recent observations suggest that the infrasound signal may carry information specific to the tornado structure and dynamics. The long propagation range of infrasound, coupled with the omnidirectional, continuous coverage provided by relatively inexpensive infrasound microphones could provide a significant improvement in our ability to

detect, track, and ultimately predict and understand tornadic phenomena, as summarized in Table 1.1. However, the limited availability and quality of tornado-relevant infrasound measurement systems, coupled with the required development effort, has prohibited the integration of these measurements into a national framework.

	Tornado	Radar	Infrasound
Horizontal coverage	Localized	Directional Sweeps	Omnidirectional
Temporal dynamics	Rapid	Periodic Scans	Continuous
Low altitude effect	Primary Location	Ground Clutter	Reflections
Core Physical Effect	Latent Heat; Wind	Moisture Reflections	Pressure Wave Propogation

Table 1.1: Infrasound has several potential advantages over existing weather radar measurements as a potential mechanism for tornado detection and tracking

Currently available tornadic infrasound data remains sparse, which has prevented the identification of the fluid mechanism responsible for its production. To increase the probability of detection and demonstrate real-time tornado infrasound processing, this thesis adapts fixed infrasound sensing technology to equip storm chasers that are in regular proximity to tornadoes with mobile infrasound measurement capabilities. This system has and continues to increase the quantity of samples while also reducing the long-range propagation-related uncertainties in the measurement analysis. This thesis describes the design and deployment of the Ground-based Local INfrasound Data Acquisition (GLINDA) system that collects and relays data from measurement devices including a specialty infrasound microphone, GPS receiver, and an IMU to a secondary processing computer board located off-board. GLINDA has been deployed with storm chasers beginning in mid-May of 2020 and has sampled several severe weather phenomena, including an EFU tornado in Lakin, KS. The acoustics measured from the EFU tornado have an elevated broadband signal between 10 and 15 Hz, which is consistent with past observations from small tornadoes. In contrast, a significant hail event produced no notable infrasound signal compared to the spectra before and after the event, even with rotation in the storm, which is also consistent with past observations. These consistent observations demonstrate the ability to acquire

valuable tornado infrasound observations from this mobile system and the capabilities for real-time processing of data sets going forward.

This thesis is organized into four chapters. Chapter 1 reviews project motivations and relevant literature on tornado infrasound, modelling, and system identification approaches. Chapter 2 covers the design, development/deployment, and analysis of a portable infrasound measurement tool carried by stormchasers for real-time monitoring of tornado infrasound. Chapter 3 applies a frequency response magnitude system identification frameworks to generate candidate models of tornadic infrasound production mechanisms via measured tornado acoustic measurements and selected wind noise models from literature. Chapter 4 reviews the thesis' primary contributions and conclusions, acknowledges limitations to the study, and provides suggestion for future works.

1.2 Literature Review

1.2.1 Tornado Infrasound

The tornado-infrasound production hypothesis first appeared in 1960's conferences and only a minority of early work is available in archival journals [21]. Contemporary tornado infrasound results continue to be reported primarily in conference papers [7; 8; 39; 47], project reports [52], and oral presentations [24; 51]. Exceptions to this trend include four journal articles focused on infrasound observations from tornadoes [6; 15; 16; 18]. Bedard [6] showed that 1 Hz infrasound emissions followed the available radar observations associated with a tornado. Bedard [6] also indicates that over 100 infrasound signals from the NOAA Infrasound Network (ISNET) were determined to be associated with tornado and tornado formation processes; the details of the association technique are not included in the article. Frazier et. al [18] tracked tornadoes in Oklahoma using beamforming at infrasound frequencies. Dunn et. al [15] detected a 0.94 Hz acoustic signature associated with an EF4 tornado in Arkansas

using a ring laser interferometer.

Systematic infrasound observations from tornadoes and their formation processes remain a research challenge, which continues to contribute to large uncertainties associated with the observations and the underlying fluid mechanism responsible for its production [44]. The need for detailed tornado related infrasound observations appropriate for archival literature motivated an effort to increase both the number and quality of tornado infrasound observations, beginning with the 2016 installation of a fixed, 3-microphone infrasound array on the Oklahoma State University campus. The OSU fixed array observations have provided some of the most recent and complete tornadic infrasound measurements, including infrasound associated with the 11 May 2017 EFU tornado [16]. The fixed nature of this array limited the proximity to tornadoes and radar sites, and though 2019 included a historically high number of tornadoes, only a few observations had both reliable infrasound and radar data [37]. To address this gap, a mobile 4-microphone infrasound array was developed [42], heliotrope solar hot air balloons [9] were equipped with infrasound sensors [62], and a Ground-based Local INfrasound Data Acquisition (GLINDA) system was developed to be carried by storm chasers. The result is a robust ecosystem of complementary measurement technologies that are capable of improving the number and quality of infrasound measurements near tornadoes.

1.2.2 Tornado Modelling

The topic of modelling tornado dynamics remains an open research problem. Rotunno [54] remarks of this, "Most of what is known of the fluid dynamics of tornadoes derives from laboratory and numerical experiments that produce vortices that share similarities with what can be observed in a tornado." In this regard, vortex chambers have been used to simplify and select aspects of supercell structures which may produce tornado. Here a cursory overview of two of the more influential chamber structures

is presented with a discussion below of their limitations – the laboratory experimental model developed by Ward [63] and later revised by Church et. al [10; 11], and the Fiedler chamber which is utilized for a series of numerical experiments. These models were scaled and validated with parameters such as swirl ratio from tornado measurements in literature and photographic evidence [54]. The infrasound acoustic output has generally not been scaled to these models due to lack of comparable, robust field measurements. Additionally difficult in applying these modeling approaches to real-time forecasting of tornadic events is the often prohibitory physical and time constraints associated with the problems. This indicates an area where simplified dynamic models representing the significant physical modes returned from system identification can open new areas of analysis.

1.2.2.1 Ward Chamber

The experimental design of the Ward chamber allows for representation of the supercell updraft via an upward-directed fan located centrally in a cylindrical sealed volume where angular momentum is induced via an internal rotating screen as seen in Figure 1.1 (a). The working fluid is assumed to have constant density and dynamic viscosity which allows for its characterization by only its kinematic viscosity. This assumption leaves a series of six external dimensional parameters: r_0, r_s, h, v, and Γ representing radius of the orifice, radius of the rotating screen, depth of the representative inflow layer, kinematic viscosity, and circulation respectively. Notably, Ward type chambers are associated with small values of $a \equiv h/r_0$ and $r_0/r_s \approx 1/2$ [54]. Due to the presence of open boundaries with no known flow, this representation of a tornadic structure produces significant challenges for extension of the analysis [54].

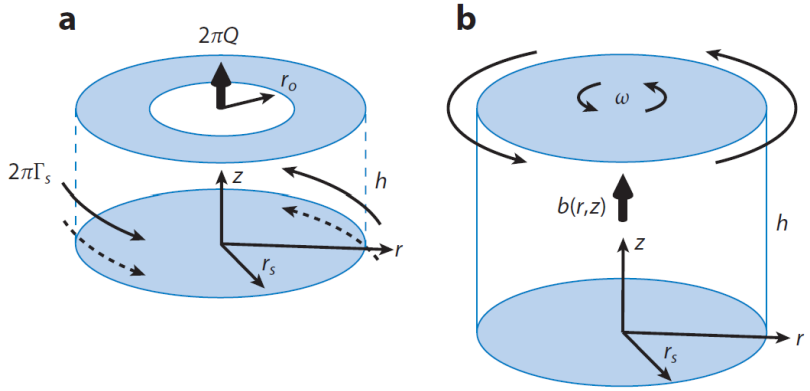

Figure 1.1: Vortex chambers discussed (a) Ward 1972 [63] (Adapted from Davies-Jones [14]) and (b) Fiedler 1995 [17]

1.2.2.2 Fiedler Chamber

To combat the issues of the open boundary with unknown flow inherent to the Ward chamber, Fiedler [17] proposed an idealization for updraft as a closed domain containing ambient rotation (figure 1.1 (b)). For the proposed model, the height of the chamber encloses the entire updraft of the thunderstorm and represents the distance between the ground and tropopause. The rotation of this region then corresponds to the entire column of rotating updraft in a supercell thunderstorm. The Fiedler chamber solutions are then dependent on two nondimensional numbers - the swirl ratio $\Omega = \omega h/W$ where W is the velocity scale defined by the buoyancy force per mass unit (equation. 1.1) and a Reynolds number defined by $Re_F = Wh/v$.

$$W = \sqrt{2 \int_0^b b(r,z)|_{r=0}\, dz} \tag{1.1}$$

As the numerical analysis solves a low-pass filtered Navier-Stokes equation through CFD, runtime considerations cannot be neglected in context of applying these models to real-time measurements made on the ground near a tornadic event.

1.2.2.3 Infrasound Production Hypotheses

Petrin and Elbing [43] compiled a list of potential acoustic mechanisms which may be associated with tornadic infrasound production (Figure **??**). Latent heat sources [2], aeroacoustic jet noise [18], radial oscillations [1; 6], and non-equilibrium effects have all been posited and correlated to either observations or numerical results, however, none of these approaches fully describes the tornadic infrasound signatures as measured.

Mechanism	Likelihood	Reason
Electromagnetic	Unlikely	All known EM sources are impulsive
Aeroacoustic Sources: Co-rotating vortices	Unlikely	Expected frequency would be lower than observations
Aeroacoustic Sources: Vortex-surface-interactions	Unlikely	Not possible prior to tornado making contact with the ground
Aeroacoustic Sources: Turbulent Jet Noise	**Likely**	Likely a higher frequency signature, which can be predicted using a modified model of aeroacoustic jet turbulence
Aeroacoustic Sources: Radial vortex vibration	**Possible**	The effect of non-columnar structure must be incorporated
Latent Heat Sources	**Likely**	Simulations indicated latent heat is required and its is produces infrasound in the 1-10 Hz frequency range
Non-equilibrium Effects	**Possible**	The modified N-S equation has predicted tornado flow-fields and a mechanism for sound propagation, though the scaling has not been explored

Figure 1.2: Discussion of potential acoustic mechanisms associated with tornadic infrasound production - Petrin and Elbing 2017 [43]

1.2.3 System Identification

System identification can be considered as stated by Tischler [57] - "a process that provides a model that best characterizes (in some least-squares sense) the measured response to controls." Essential to the process of system identification is the definition of inputs and outputs for the system which are identifiable and informative. Generally this requires the collection of high-quality data for input and output for the system to be identified [57]. A hypothesis for a simplified tornado acoustics block diagram can be seen in Figure 1.3. Here the selection of acoustics for output is pre-selected. As noted in White et. al [64], further simplification to the process map can be obtained

by making measurements in the near field which mitigates propagation and allows the assumption $\mathbf{P} \approx \mathbf{I}$ to be considered valid (Figure 1.4).

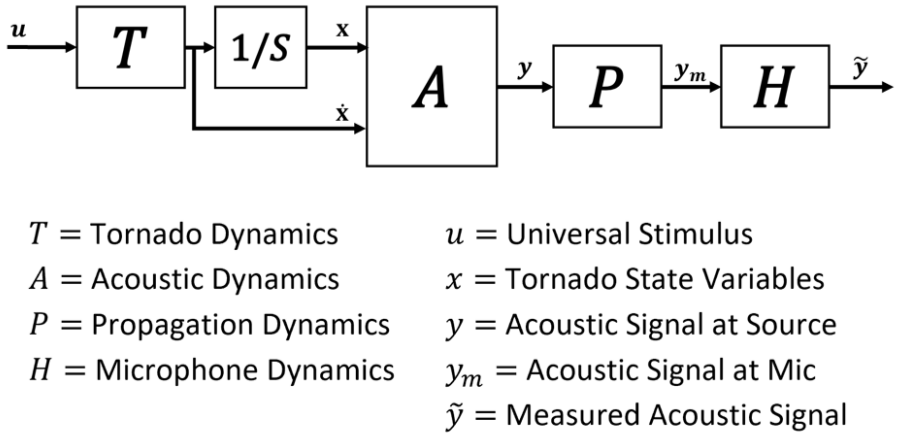

Figure 1.3: Simplified tornado acoustic block diagram showing path from universal input through measurement (White et. al [64])

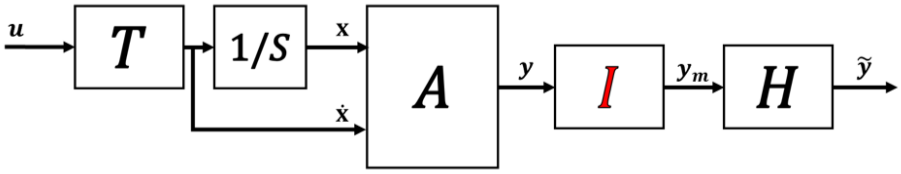

Figure 1.4: Reductions to tornado acoustic block diagram with short range measurements(White et. al [64])

Selection of input variable and collection of the associated data remains an challenge for robust system identification analysis from field measurements. Lewellen [30] determined that pressure measurements in a tornado should be made with a temporal resolution of above 1 hertz to sufficiently resolve the characteristics of a tornado, however, Karstens et. al [26] notes that only measurements from Winn [65] meet these standards for pre-2002 events. Karstens et. al [26] additionally notes that "because of the inherent logistical difficulties of placing near-ground instrumentation in the path of a tornado, only a few such measurements in tornadoes exist." Advancements for measuring apparatuses capable of operating in atmospheric conditions like tornadoes are an area of expanding research [53; 49], but insufficient data exists in relevant

environments correlated to infrasound measurements for identification of the tornado dynamics block, $\mathbf{T}$, at this time. In chapter 3, a selection of energy and pressure models will be discussed and utilized as input for the acoustic production process and subsequent analysis.

CHAPTER II

Ground-based Local INfrasound Data Acquisition (GLINDA) system

This chapter[1] focuses on the design, deployment, and recent results from the mobile stormchasing unit (GLINDA). The GLINDA unit provides a tool to mitigate uncertainties associated with atmospheric propagation by acquiring targeted close range measurements from verified tornadoes. The GLINDA unit was deployed with storm chasers (Val and Amy Castor) beginning in the 2020 tornado season, and continues to provide valuable real-time measurements.

This chapter is organized as follows. Section 2.1 outlines the design goals, design process, and calibration procedure for the GLINDA unit. Section 2.2 covers the real-time processing needs and an analysis approach to achieve those goals. Section 2.3 describes two example storm measurements (a tornado and hail-producing storm) recorded by the unit during the 2020 storm season and used to verify its operation. Section 2.4 shows calibration, spectral, and peak identification results for the installed unit and the example storms.

2.1 GLINDA Design and Calibration

In this section, system design goals are identified, and techniques for hardware components, computational platforms, and data handling for collection and retention prior to analysis.

[1]Chapter is adapted from the manuscript under review: White, Brandon C., Elbing, Brian R., and Faruque, Imraan A., *Infrasound measurement system for real-time in-situ tornado measurements* Submitted: European Geosciences Union's Atmospheric Measurement Techniques, 05/26/2021. https://www.atmospheric-measurement-techniques.net/

2.1.1 System Design

The primary measurement system goals were: (a) microphone signal resolution of 20mPa or better to provide comparable infrasound feature resolution to existing fixed arrays [16], (b) positioning resolution under 10 m to provide comparable or better accuracy to current NOAA-reported tornado coordinates, and (c) "real-time" remote data relay, where real-time is defined as at or exceeding weather radar update frequencies (approximately once per 90 seconds).

2.1.1.1 Infrasound Microphone

GLINDA uses an off-the-shelf infrasound microphone (Model 24, Chaparral Physics), the same model used for the fixed 3-microphone array near Oklahoma State University [16]. The microphone has a sensitivity of 401 mV/Pa at 1 Hz and a flat response from 0.1-200 Hz to within -3 dB (flat to within -0.5 dB for 0.3 to 50 Hz). The typical frequency response for this model of microphone is provided in Figure 2.1. The noise for this microphone at 1 Hz was -81.6 dB relative to 1 Pa^2/Hz. The microphone was mounted on the floorboard of the storm chasing truck as shown in Figure 2.2. Concerns about the ability to suppress wind noise motivated the mounting inside of the truck cab and, consequently, no additional windscreen was implemented. The maximum signal output for the microphone is 36 V peak-to-peak, and the analog output signal was sampled at 2050 Hz. By sampling at greater than 2000 Hz, GLINDA avoids aliasing in the frequency band of interest. A calm-day measurement from the system is provided as a baseline measurement in Appendix B.

2.1.1.2 Sensor Components

In addition to the infrasound microphone, GLINDA monitors and records data from an inertial measurement unit (IMU), a Global Positioning System (GPS) receiver, and the analog-to-digital converter (ADC) that was connected to the analog output

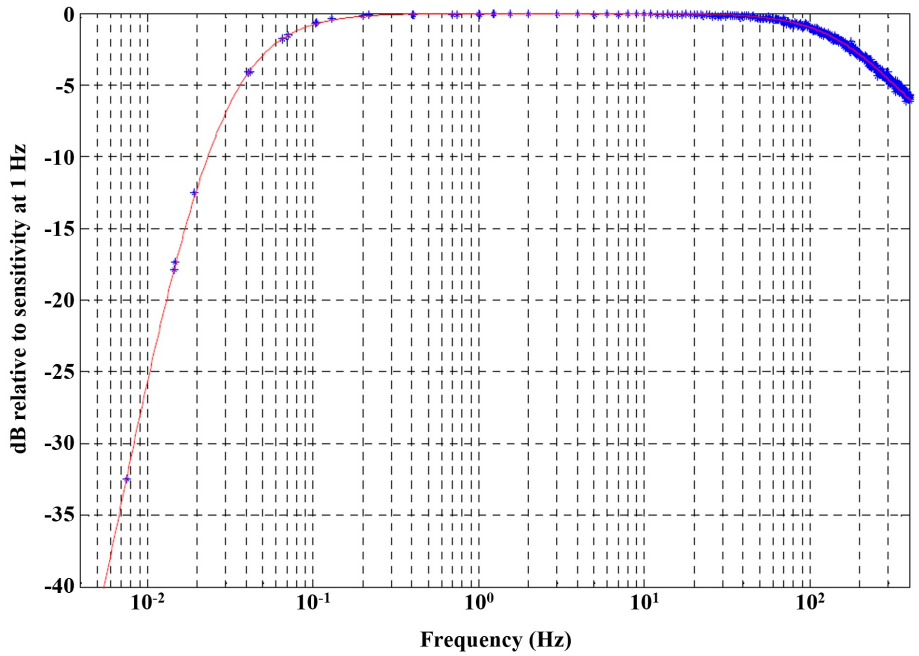

Figure 2.1: Typical frequency response curve for a Model 24 (Chaparral Physics) microphone, which was used for this deployment of GLINDA. Credit: Chapparal Physics.

Figure 2.2: Image of GLINDA-housing storm chasing vehicle showing approximate location and configuration of install.

from the infrasound microphone. An illustration of data flow for the upload process from each of the sensors is provided in Figure 2.3. The IMU, GPS, and ADC were sampled at 100 Hz, 1 Hz, and 2050 Hz, respectively. The microphone ADC (ADS1115, Adafruit Industries) has a 16-bit resolution and signal voltage tolerance of $\pm$5V, giving a quantization increment of 76μV. Since the microphone outputs a differential signal reading of 0-36 V, a voltage divider circuit was implemented with

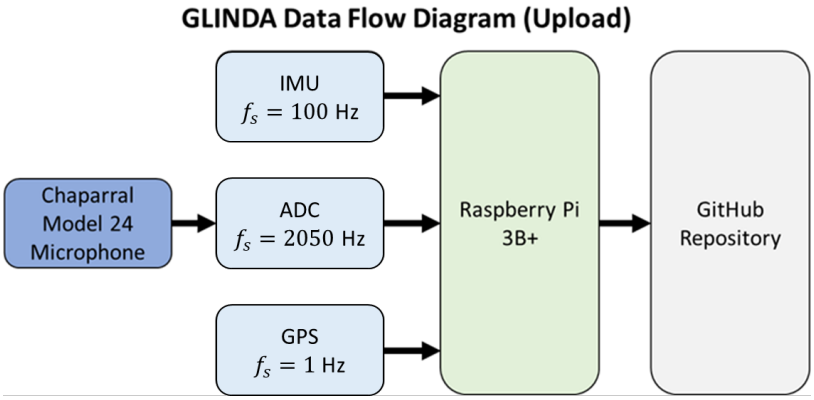

Figure 2.3: Flowchart for acquiring and uploading of data from GLINDA

gain ratio of 13.6% to ensure the measured signals fall within the ADC tolerance. The nominal microphone sensitivity of 401 mV/Pa provides a pressure resolution of 1.4 mPa, keeping GLINDA's quantization error below the existing fixed array's typical noise floor of 20 mPa observed during severe storms with high winds [16]. The GPS unit (746 Ultimate GPS Breakout Ver 3, Adafruit Industries) provides position and velocity accuracy of 1.8 m and 0.1 m/s respectively. 1.8 m radially is accurate to approximately 0.00001° for data collection latitudes. For comparison, current NOAA tornado reports typically provide GPS coordinates with three to four decimals, and the system positioning accuracy exceeds these estimates. Each measurement is time-stamped and stored locally until export processes are initiated.

2.1.1.3 Computing Platform

The mobile GLINDA hardware is built on a Raspberry Pi 3B+ platform with a Raspbian distribution. The scripts were written in Python 3.7 and implement Adafruit libraries for reading the attached sensor packages over I^2C and serial/UART connections. Upon startup, the system initializes all sensors for data collection and continues recording until loss of power. Data is saved every 10 s to ensure minimal loss in the event of unexpected shutdown. Each data file is timestamped by the local system with time coordinated via Network Time Protocol thorough the Pi board. A system

service initializes and maintains data uploads to a GitHub repository.

2.1.1.4 Installation and Deployment

For the 2020 tornado season, GLINDA measured from within the cab of a storm chasing truck operated by Val and Amy Castor (see Figure 2.2), which provided live coverage of severe storms for a local news station in Oklahoma City, OK (News 9). GLINDA was installed during the first week of May 2020. It was powered by 1500 W inverters (Strongway), which also power the vehicle's other weather observation systems. The 60 Hz signal produced by the inverters is outside of the frequency band of interest. A small port in the roof of the vehicle allowed the GPS antenna to be routed outside of the cab for improved connectivity. Data size is limited by a power switch integrated into the vehicle dash.

2.1.1.5 Data Recovery

An illustration of the data flow from download through processing is provided in Figure 2.4. GLINDA maintains an internet connection via a router in the storm chasing vehicle that is primarily used to provide live video and audio to the local news outlet during storm chases. While connected to the internet, GLINDA scans the data storage directory for new or modified files resulting from sampling of the sensor packages. An upload commit is generated to push new or updated files to the online repository (GitHub). File uploads for the system are conducted at regular intervals, typically at $\Delta t < 60$ s. Further discussion on selection for timing considerations is provided in section 3.1.

2.1.2 Calibration

To create a broadband acoustic and infrasound signal with sufficient excitation energy over the frequency bandwidth of interest, the GLINDA system was calibrated

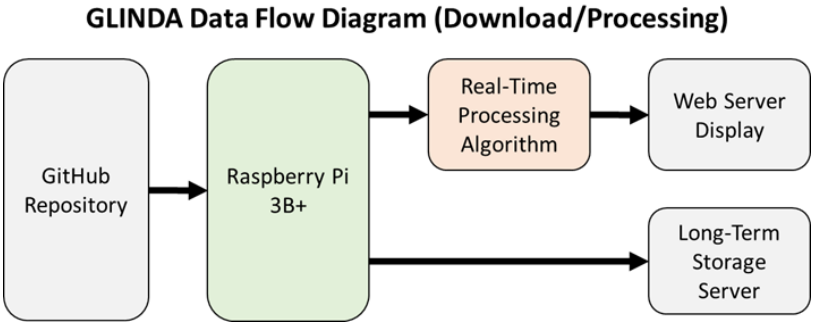

Figure 2.4: Data flow for processing, display, and storage

utilizing a series of impulsive acoustic signals generated from a 20-gauge shotgun discharged at < 2 ft range and oriented approximately 120 degrees from the unit installed in the vehicle model cabin (2019 Ford F-150). A gunshot was used to generate the impulsive signals of the test to generate significant acoustic and infrasonic spectra with similar magnitude. Two series of three gunshots were completed in cabin configurations of windows up and down. The gunshots from each configuration were then compiled into a single data series for frequency domain analysis using approximately 1 s sections of recording containing each shot (approximately 0.1 s ringing). By comparing the signal measured outside of the vehicle to the interior microphone signal, an experimental transfer function was identified for the acoustic impact of the vehicle over the frequency band of interest. A frequency domain model fit to the magnitude measurements was used as the transfer functions for the window up and down cases.

2.1.3 Real-time display interface

To provide continuous monitoring and rapidly identify temporal trends in acoustic measurements allowing storm chasers to include infrasound signals in tactical decision-making, a web interface was developed that displays the GLINDA measurements in near real-time (Fig 2.5). The primary visualizations of the data are a spectrogram displaying near real-time frequency decompositions and a maps API displaying the location of the storm chasing unit via GPS. In addition to visualizing current mea-

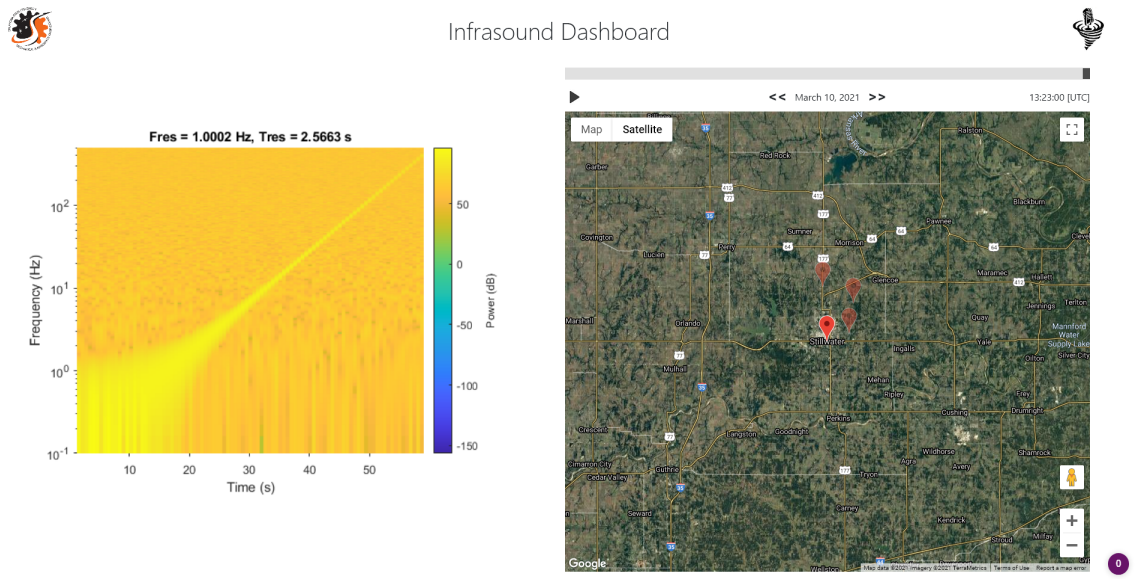

Figure 2.5: Example visualization of GLINDA-monitoring web interface

surements, a slider for time and date allows browsing historical data.

2.2 Analysis approach

In this section, a real-time analysis approach is developed that provides high-resolution spectral measurements over the region of interest, and provides robust peak-detection and finding routines.

2.2.1 Real-Time Processing Qualifications

Traditional weather monitoring of severe weather, such as tornadoes in the United States, is completed via radar analysis. The United States National Weather Service (NWS) utilizes a wide-spread network of weather radars (most notably Weather Surveillance Radar, 1988 Doppler or WSR-88D) to provide the most accurate and frequent images available [61]. Development of scanning methods that decrease time intervals between low-angle atmospheric sweeps for the WSR-88D have been the subject of repeated study and implementation [13]. The current methodology for minimizing the interval between scans is the Multiple Elevation Scan Option Supplemental

Radar Measurement Method	Update Time (s)
Full Volume Scan - WSR-88D	270
0.5^o Scan, SAILS(x1) - WSR-88D	147
0.5^o Scan, SAILS(x2) - WSR-88D	108
0.5^o Scan, SAILS(x3) - WSR-88D	89

Table 2.1: Average minimum wait time between low-inclination update scans for varieties of WSR-88D scanning methods

Adaptive Intra-Volume Low-Level Scan or MESO-SAILS. The average time between MESO-SAILS scans at the 0.5 degree radar inclination is provided in Table 2.1 and implies that GLINDA should target measurement intervals of $\Delta T_m \leq 90$ s to be comparable with current radar technology.

The update rate requirements (> 90 s), data generation rate, and desired bandwidth usage is used to identify the maximum length of an individual recorded segment that keeps pace with radar as

$$89 \geq \Delta T_t = \Delta T_m + \Delta T_u = \frac{R_G \Delta T_m}{0.1 R_u} + \Delta T_m, \tag{2.1}$$

where R_G is the rate of sensor data production, R_u is the minumum connection speed expected, total time between measurements (ΔT_t) is the sum of the time interval of data collection and the time required to upload the data (ΔT_u), and GLINDA data usage is limited to less than 10% of the available bandwidth. For the GLINDA unit, $R_G = 70$ Kb/s and the upload constraint is $1.35\Delta T_m \leq 89$ seconds.

2.2.2 Spectral transformation

In 2020, GLINDA recorded several chases during severe weather events, including a dust storm, gustnado, and significant hail events. This paper analyzes the data acquired during a tornado-producing supercell including tornadogensis and a severe hail event without tornadic activity. Traditionally the frequency decomposition of

a time-domain signal is performed using a Fast Fourier transform (FFT) that gives fixed frequency domain resolution over the 0 Hz to the Nyquist frequency ($\approx$ 1000 Hz) range. For the oversampled case, a large number of these points would be outside the frequency band of interest. In this study, we used the oversampling to reduce the frequency domain error by implementing a Chirp-Z transform (CZT) to allow the frequency domain resolution to be directed only across a desired frequency band [48], which is advantageous because the frequency band of interest for the current work is a relatively small fraction of the band returned by the FFT ($\leq 10\%$). Thus the CZT produces higher resolution over the desired range relative to an FFT. The CZT also has the advantage of reducing the required processing time given the narrowed band, which is critical for enabling real-time analysis of infrasound measurements. However, due to the data sizes presented in the current study the CZT and FFT had negligible runtime differences. The CZT, defined in equation 2.2, takes a time domain series of N points, $x(n)$, and transforms it into the complex Z-domain at a finite number of points along a defined spiral contour $z(k)$ returning frequency domain signal, $X(k)$. Here $z(k)$ is a function of a complex starting point A, the complex ratio between points W, and the number of spiral contour points M. For storm analyses over expected frequency bands previously associated with tornadic acoustics, a complex spiral was defined as given in equation 2.3, which corresponds to a band of 1-250 Hz with a frequency resolution of $\Delta f = 0.125$ Hz. A ten minute selection of microphone data was selected from one hour before the event, spanning the event, and one hour after the event for each case presented. The ten minute intervals were windowed using Hanning windows with 60% overlap and segmented into 15 s lengths.

$$X(k) = \sum_{n=0}^{N-1} x(n) z(k)^{-n},\ z(k) = AW^{-k} k = 0, 1, \ldots, M-1 \tag{2.2}$$

$$A = e^{2\pi i/1000},\ W = e^{(2\pi/1000)(249/2000)i},\ M = 2000 \tag{2.3}$$

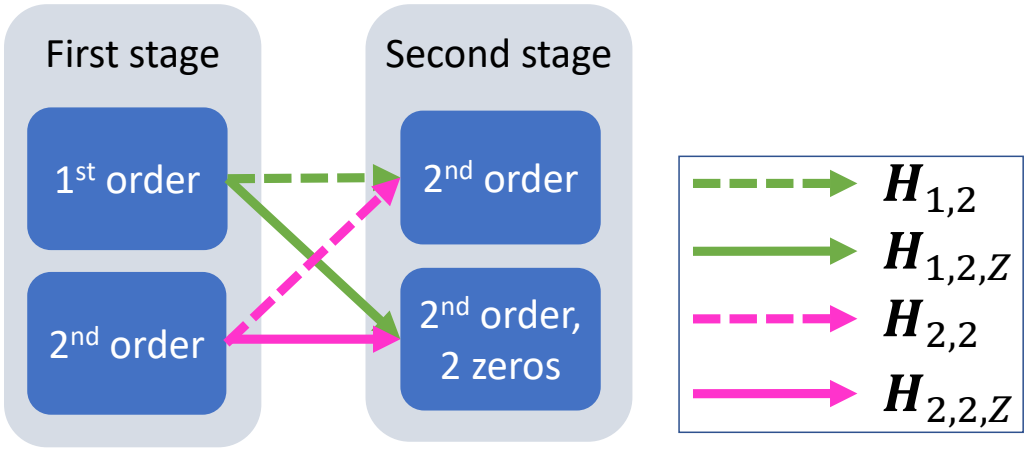

Figure 2.6: Frequency domain model structures considered and two-stage model fitting process.

2.2.3 Peak identification

To robustly identify the frequency domain peak in real-time, a model-based approach was taken using a two-stage process to compare magnitude fits to the four frequency domain model structures shown in Figure 2.6. Each fit was derived by minimizing the mean-squared error (MSE) between the measured SPL ($\tilde{Y}$) and frequency response magnitude of the transfer function ($|H|$) as Eq 2.4.

$$MSE = \sum_{f=0.1\,\text{Hz}}^{100\,\text{Hz}} (\tilde{Y}(f) - |H|(f))^2 \tag{2.4}$$

2.3 Observations

In this section, two significant weather events measured by GLINDA during the Spring 2020 tornado season and selected for detailed analysis in this study are described.

2.3.1 Tornado Event (22 May 2020)

A cold front that pushed in from the northwest of Kansas late on 21 May 2020 and into the early hours of 22 May 2020 produced several severe storms. One storm, pictured

in Figure 2.7, produced a tornado near Lakin, Kansas. The tornado touchdown at 0011 UTC at coordinates (37.802, -101.468) and ended at 0024 UTC at coordinates (37.7982, -101.4387). It was 2.83 km (1.76 miles) in length, had a maximum damage path width of 137 m (150 yards), and was classified as an EFU by the NWS because it tracked over an open field that produced insufficient recorded damage for reliable categorization [35]. The storm chasers, equipped with GLINDA, intercepted the tornadic storm system shortly prior to tornadogenesis. The intercepting storm chasers were located approximately 4 km SSE of the tornado during tornadogenesis.

Figure 2.7: (Left) Picture of the storm system that produce the tornado near Lakin, KS on 22 May 2020. (Right) Picture of the Lakin, KS tornado. Photo credit: Val and Amy Castor.

2.3.2 Large Hail (22 May 2020)

The day after the Lakin EFU tornado, a stalled outflow boundary intersected a dry-line resulting in the firing of numerous severe thunderstorms. One of these large supercell storms produced baseball-sized hail as it moved over southern Oklahoma. The GLINDA equipped storm chasers intercepted the storm as it moved through Comanche County and produced 25.4 mm (1 inch) hail at 2315 UTC on 22 May 2020 near the coordinates (34.62, -98.75) [36]. This storm did exhibit weak rotation at times, but a tornado was never produced.

2.4 Results

In this section, the calibration results are presented, the frequency domain analysis of the two storms are compared, and the peak finding routine is applied to signals with an infrasound rise. The spectral comparison shows a rise in infrasonic signals in the presence of a tornado-producing supercell near tornadogenesis. The rise is statistically significant with respect to the signal noise and standard deviation, and does not appear after the tornado or in a non-tornadic hail storm which contained rotation.

2.4.1 Calibration

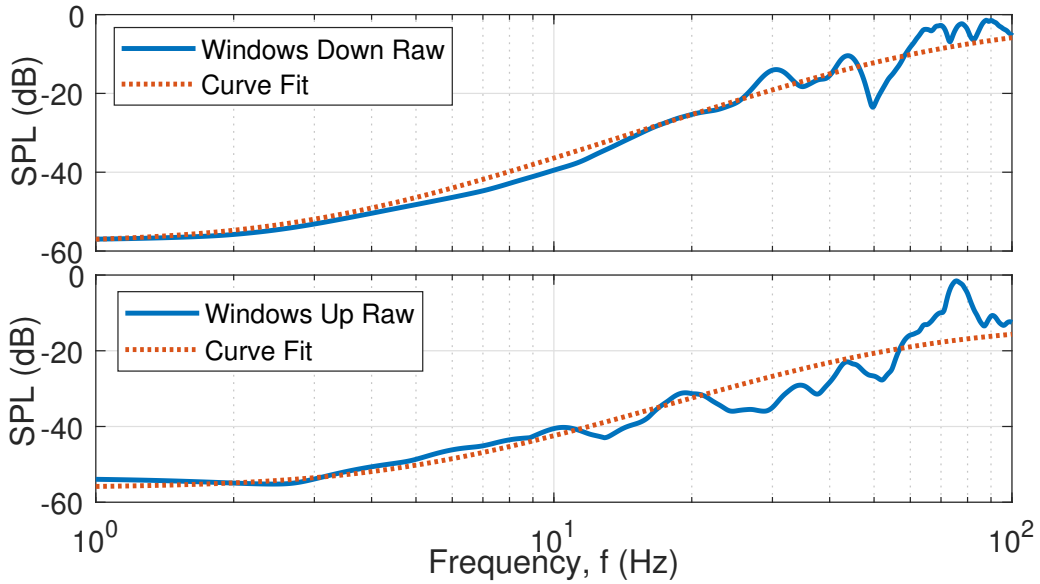

Figure 2.8: Experimental transfer function data and fitted models for windows up and windows down configurations

Figure 2.9 provides the measured frequency response as obtained through calibration described in section 2.1.2 for a windows up and down configuration. A frequency domain model fit to the magnitude measurements then gives transfer functions $H_u(s)$ and $H_d(s)$ for the window up and down cases (Equations 2.5 and 2.6), respectively. These transfer functions are compared in Figure 2.9.

$$H_u = \frac{0.22(s+31.5)^2}{(s+377)^2} \tag{2.5}$$

$$H_d = \frac{0.79(s+18.8)^2}{(s+471)^2} \tag{2.6}$$

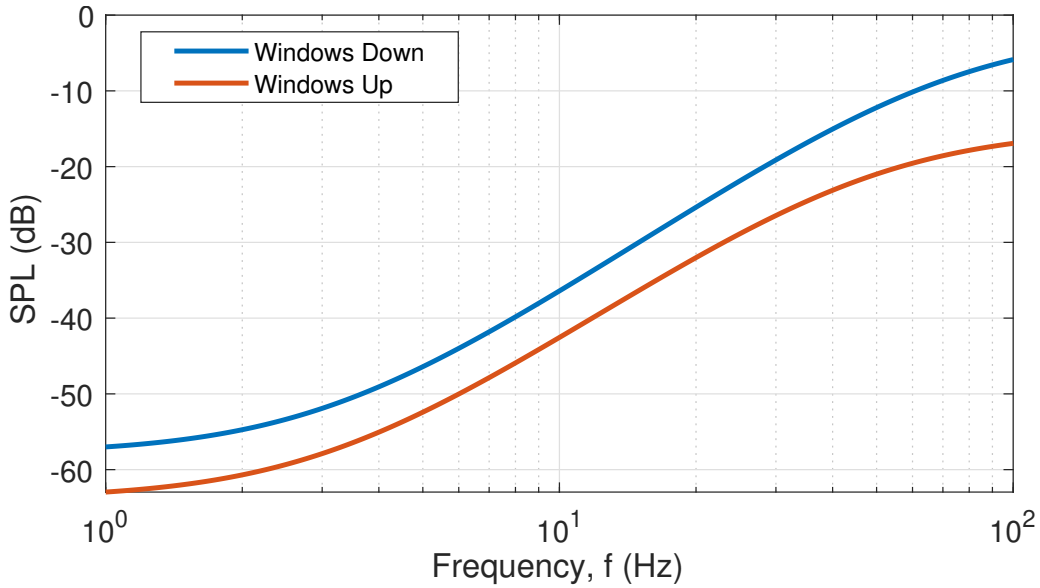

Figure 2.9: Comparison of models for windows up and windows down configurations

The spectral analysis and peak finding algorithm in section 2.4.3 is discussed relative to the recorded signal (as implemented in the real-time workflow). This implementation neglects the calibration of the truck bed. For analysis of the underlying physical mechanisms responsible for tornado infrasound or for comparison between multiple units, the truck's acoustic response may be removed by applying the inverse of the calibration transfer function.

2.4.2 Spectral results

The spectral contents recorded on GLINDA before, during, and after the Lakin tornado are compared in Figure 2.12. To reduce the effect of the significant spectral slope, a linear regression was computed as SPL change (dB) per frequency decade for pre-, post-, and during event conditions as defined in equation 2.7 and over the

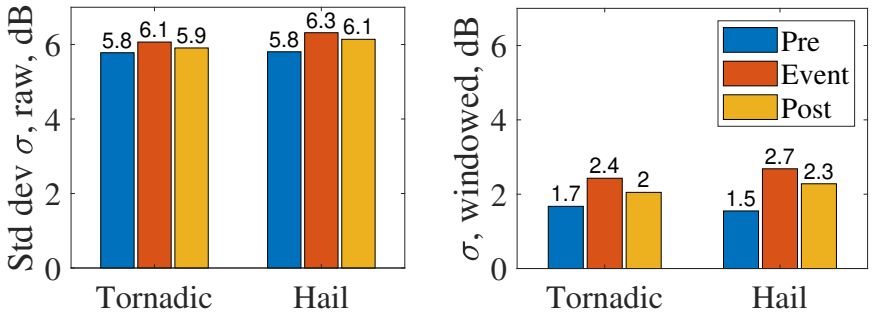

Figure 2.10: Standard deviation of spectra

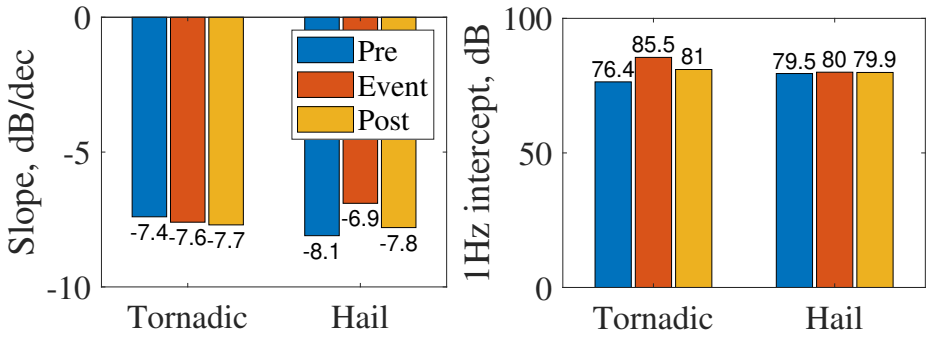

Figure 2.11: Linear fit parameters

frequency range of [1, 250] Hz. The trendlines have slopes within 0.5 dB/decade of each other as shown in Figure 2.11, while the varied 1 Hz intercepts also suggest an overall rise in spectral energy content across the band of interest during tornado interception. Acoustic work often associates broadband SPL rise below 500Hz with wind [31; 32; 34], which does not necessarily extrapolate to the sub-acoustic region under consideration here.

$$\hat{X}_{SPL}(f) = a_0 \log_{10}(f) + a_1 \tag{2.7}$$

The variance about the best fit curve for each case illustrates the noise reduction in frequency domain due to windowed averaging. The raw and windowed variances for the pre-, post-, and during tornado intervals are provided in Figure 2.10. This comparison shows that the frequency-domain averaging provided by windowing reduced the numerical variance from 33-35 dB in the raw transform to 2.9-5.9 dB variance in the windowed transform. This noise reduction significantly improves the ability

to resolve features with changes in the 3-6 dB magnitude range. From this variance reduction, the elevated signal in the 10 to 15 Hz frequency band during the tornado is made more apparent. The center of this frequency band (10-15 Hz) shows a 9 dB rise above the linear fit, and this rise over this frequency band is not present one-hour prior to or one-hour following the tornadic activity.

The 10-15 Hz elevated frequency band during the tornado accounts for 3.3 dB (and therefore the majority) of the variance during the tornadic event and the peak falling within this range is consistent with this being a relatively small tornado. Tornado infrasound is consistently reported with a fundamental frequency in the 0.5 to 10 Hz range [6] with the smaller the tornado the higher the frequency. Elbing et. al [16] observed a similar small EFU tornado and its fundamental frequency was estimated to be 8.3 Hz. These observations are nominally consistent with the analysis of Abdullah [1] that predicts $f_n = (4n + 5)c/4d$, where f_n is the frequency of mode n, c is the speed of sound, and d is the diameter of the vortex core. There are fundamental issues with this analysis, but all of the results published in archival journals [6; 18; 15; 16] nominally follow this trend (though generally aligning better with the first overtone, $n = 1$). Thus it is appropriate to use this relationship as a nominal empirical relationship. This analysis predicts that a tornado with a fundamental frequency of 12.5 Hz would have a vortex core diameter of 34 m. Past observations indicate that this estimate is likely to be low and the actual tornado core that would produce a 12.5 Hz fundamental frequency would fall in the range of 35-90 m. This is still below the reported maximum damage path width (137 m). However, having a similar magnitude is likely all that can be expected given the uncertainty in the analysis, damage assessment (both estimated values as well as only reporting the maximum), and relationship between vortex core and damage width. Note that the largest tornadoes have core diameters well in excess of 1000 m [59; 60].

The spectral content associated with the Commanche County hail event is shown

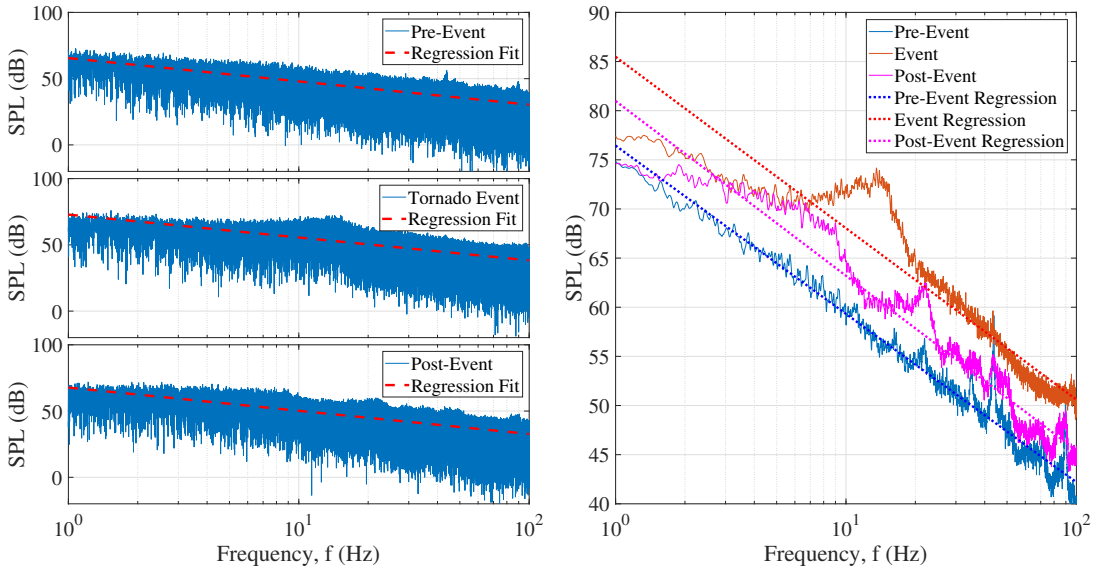

Figure 2.12: Frequency domain GLINDA data during the Lakin, KS tornadic event that occurred from 0011 UTC to 0024UTC on 22 May 2020

in Figure 2.13. As with the Lakin tornado analysis, calculation of best fit lines (defined in equation 2.7 with fitting parameters listed in Figure 2.11) show over 30 dB reduction for windowed spectra as listed in Figure 2.10. The linear best fit lines for the hail event do not show significant SPL differentials between the three intervals (pre-, post-, and during the hail) at the lower end of the measurement range < 10 Hz. The slope of the fit during the hail event is 3 dB/decade higher than the pre- or post-events which creates a SPL difference of up to 5 dB over the band of interest. Unlike the Lakin EFU tornado, there was no clear rise in SPL in the 10 to 15 Hz band. However, smaller rises near 50 and 80 Hz for the event spectra are present with a peak of 6 dB relative to the linear best fit. It is unclear what is responsible for these peaks, but these features are at frequencies above what is typically associated with severe weather (though some overtones have produced signals in the audible range). In the frequency range of interest (nominally 1-10 Hz), there is no apparent signal that was produced. This is consistent with past observations that have noted that hail producing storms without tight rotation typically do not produce an infrasound signal [44].

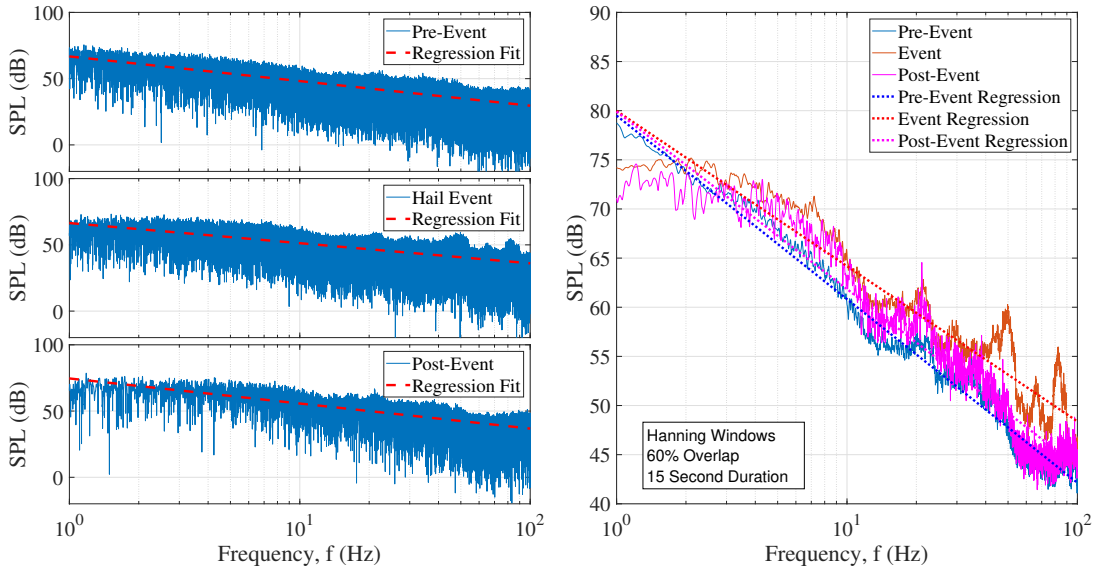

Figure 2.13: Frequency domain infrasound measured with GLINDA during the Comanche County hail event at 2315 UTC on 22 May 2020.

TF Form	MSE (dB^2)
$k_0 + \frac{a_1}{s}$	6.98
$\frac{a_0}{s + a_1}$	3.28
$\frac{a_0}{s^2 + a_1 s + a_2}$	5.31
$\frac{a_0}{s^3 + a_1 s^2 + a_2 s + a_3}$	(Did not converge)

Table 2.2: Mean-Squared Error for various first stage curve fits to raw data

2.4.3 Peak identification results

For the tornadic measurements, an infrasound peak was present and the results of the two-stage model fitting process in Figure 2.6 are presented in Tables 2.2 and 2.4.

From the first stage model fits, a first order fit has the lowest mean-squared error (MSE) between the tested transfer function models. The first order model and second order model were further investigated through a second stage transfer function model fitting. To develop the second grouping of models, the difference between the raw data and the first stage models was compared to an more select group of transfer functions based on observable characteristics in the resulting difference signal - namely the rise

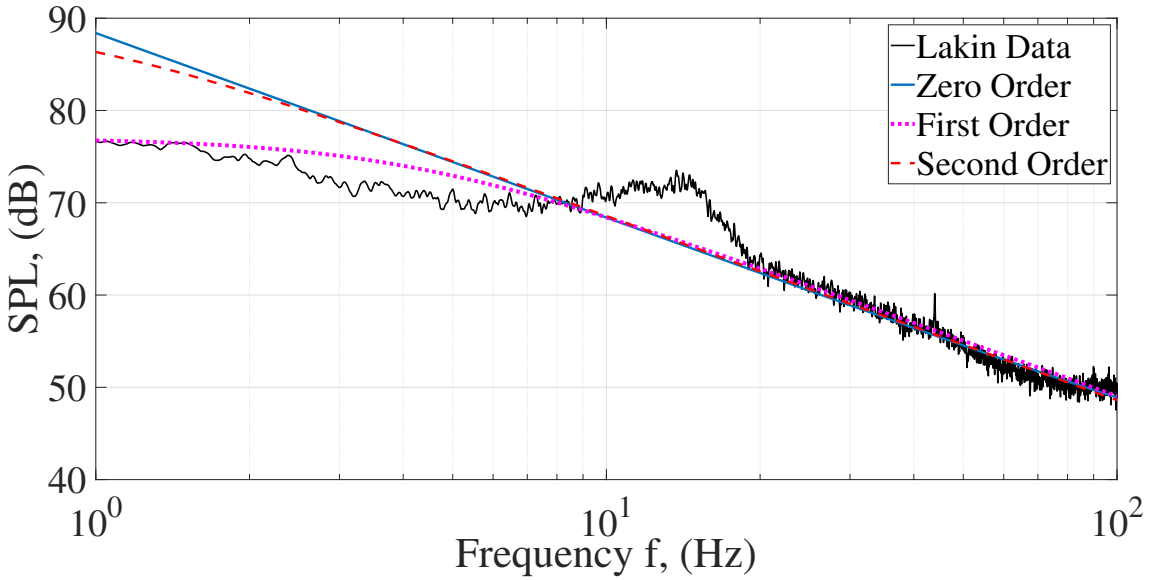

Figure 2.14: First stage model fit to Lakin, KS tornado infrasound/low-sonic measurements

over the 10-15 Hz band and the flat region in the audible range. Results of the overall model fits comprised by adding the fitted models from the secondary analysis to the first stage model fit are presented in Table 2.3 where values of the percent errors for detected frequency for the peak (Eq 2.8) and detected peak magnitude (Eq 2.9) were calculated relative to manually gathered values. The MSE for the combined fits is additionally presented.

$$E_{f_p} = |\frac{f_p - \hat{f}_p}{\hat{f}_p}| \tag{2.8}$$

$$E_{|H|_p} = |\frac{|H|_p - \hat{Y}_p}{\hat{Y}_p}| \tag{2.9}$$

The model structure fitting process is a nonlinear minimization that is prone to local minima or poorly fit terms. To examine the robustness of the model fits to differing initial guesses, a Monte-Carlo approach to fitting model uncertainty was implemented by taking one thousand initial parameter guesses uniformly distributed over one order of magnitude surrounding what is an expected range of values.

Although $H_{2,2,Z}$ has the lowest overall MSE and percent error for peak magnitude, the coefficients returned by the optimization process are of large order and have

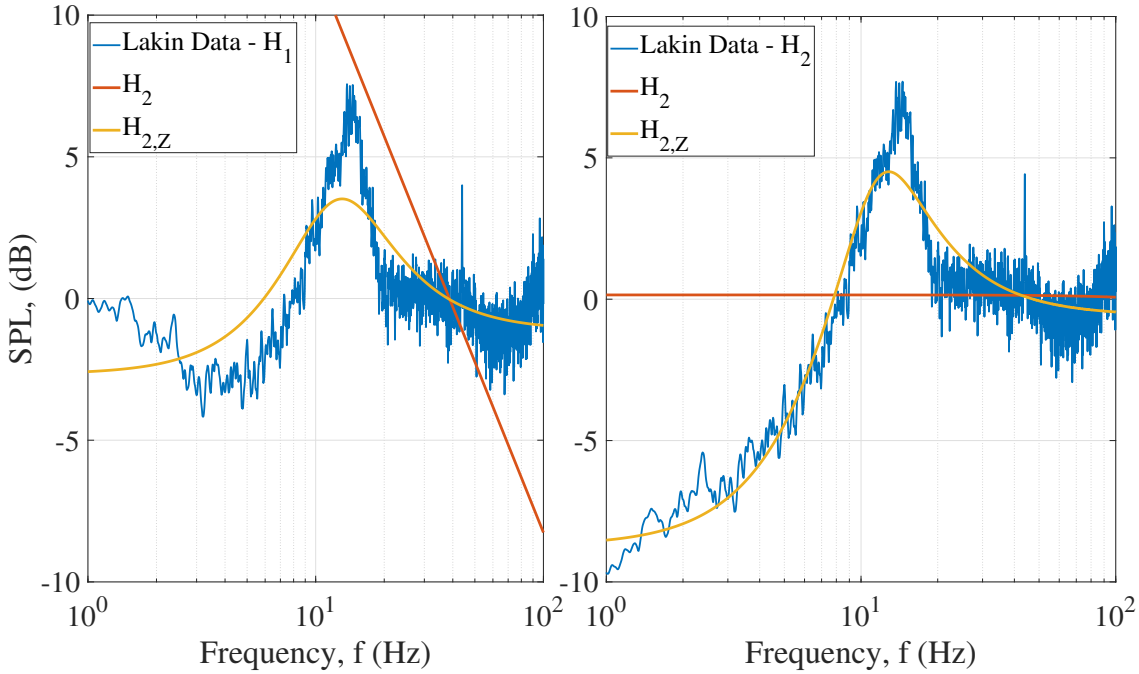

Figure 2.15: Secondary curve fits to Lakin, KS tornado measurements with select first stage fits subtracted

significantly larger adjacency value bounds as compared to first stage, first order fits creating over-fitting concerns (Table 2.4). $H_{1,2,z}$ by contrast does not produce similarly large coefficients and low adjacent value bounds. These fit parameters are achieved while only producing a 3 percentage point increase in the peak percent error and 0.8 dB^2 mean square error over the frequency band suggesting it may be a more viable model candidate. An additional round of fits was completed for the $H_{1,2,Z}$ model structure implementing a log frequency weighting to the mean-squared error formulation in 2.4 as a decadal Gaussian distribution centered on $f = 10$ Hz. The weighting scheme decreased $E_{|H|_p}$ by 12% in exchange for f_p and MSE increasing 3%. Because the focus of this modelling approach is largely concerned with peak frequency identification, the usage of this weighting method was not further implemented for usage in real-time operation. In alternative operation concerned more with peak magnitude identification, this presents a potentially appealing alternative to unweighted MSE minimization approaches.

Fit Name	Stage 1	Stage 2	$\mathbf{E}_{\mathbf{f}_{\mathbf{peak}}}$ (%)	$\mathbf{E}_{\mathbf{\lvert H\rvert}_{\mathbf{peak}}}$ (%)	**MSE** (dB^2)
$\mathbf{H}_{1,2}$	$\frac{a_0}{s+a_1}$	$\frac{b_0}{s^2+b_1s+b_2}$	99.3	111.4	64.9
$\mathbf{H}_{1,2,Z}$	$\frac{a_0}{s+a_1}$	$b_0\frac{(s+b_1)^2}{s^2+b_2s+b_3}$	6.6	8	1.82
$\mathbf{H}_{2,2}$	$\frac{a_0}{s^2+a_1s+a_2}$	$\frac{b_0}{s^2+b_1s+b_2}$	99.3	45.9	5.32
$\mathbf{H}_{2,2,Z}$	$\frac{a_0}{s^2+a_1s+a_2}$	$b_0\frac{(s+b_1)^2}{s^2+b_2s+b_3}$	8.2	5.3	1.08

Table 2.3: Fit parameters for the four model structures.

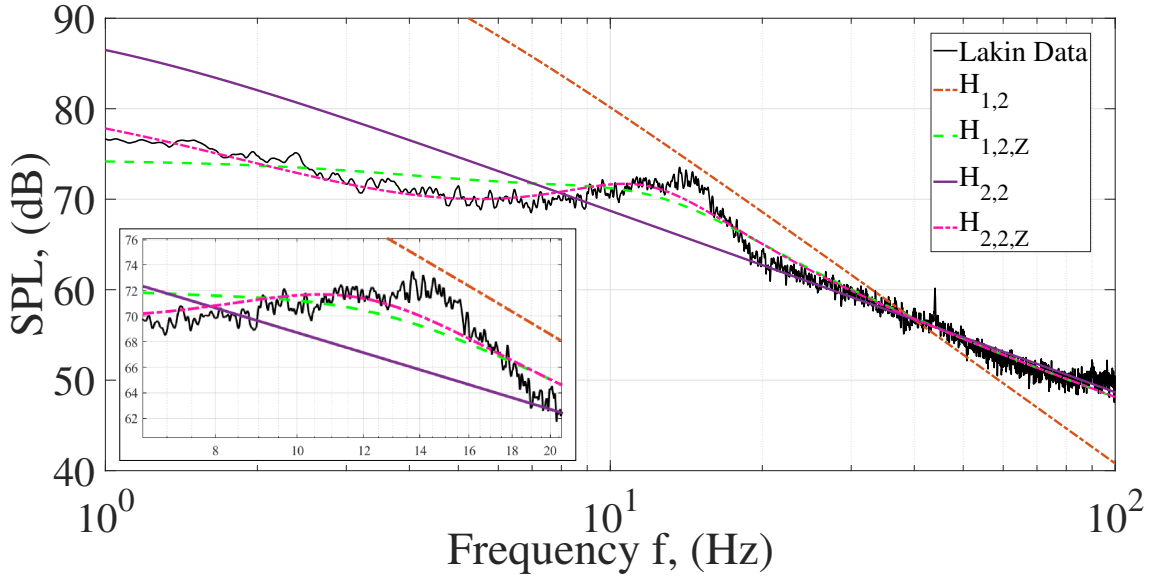

Figure 2.16: Comparison of frequency-domain model fits to Lakin, KS tornado measurements

		a_0	a_1	a_2	b_0	b_1	b_2	b_3
$H_{1,2}$	Median	1.78×10^5	25.15	–	1.43×10^5	549	2.5×10^4	–
	Adjacent Values	$\pm 10^{-4}\%$	$\pm 4 \times 10^{-5}\%$	–	$\pm 10^{-4}\%$	$\pm 10^{-4}\%$	$\pm 4 \times 10^{-4}\%$	–
$H_{1,2,Z}$	Median	1.78×10^5	25.15	–	0.879	72.411	85.408	6266
	Adjacent Values	$\pm 3 \times 10^{-6}\%$	$\pm 3 \times 10^{-5}\%$	–	$\pm 3 \times 10^{-6}\%$	$\pm 3 \times 10^{-5}\%$	$\pm 4 \times 10^{-5}\%$	$\pm 10^{-4}\%$
$H_{2,2}$	Median	8.53×10^{12}	5.4×10^7	4.1×10^5	1.3×10^5	464	2.5×10^4	–
	Adjacent Values	$\pm 450\%$	$\pm 415\%$	$\pm 5.5 \times 10^3\%$	$\pm 39.9\%$	$\pm 58.4\%$	$\pm 4 \times 10^{-4}\%$	–
$H_{2,2,Z}$	Median	9.2×10^{12}	4.7×10^7	2.5×10^4	0.934	45	56.2	5529
	Adjacent Values	$\pm 386\%$	$\pm 466\%$	$\pm 7.9 \times 10^5\%$	$\pm 9.1\%$	$\pm 113\%$	$\pm 95\%$	4.6%

Table 2.4: Median fit parameters uncertainty distribution as quantified by Monte Carlo convergence over one thousand initial guesses

CHAPTER III

Experimental Identification of Tornado Acoustic Production Dynamic Model

In the previous chapter, a set of transfer function candidates were presented which correspond to an assumed uniform input across the frequency band, however, this was assumed without discussion. In this chapter a more systematic review of problem formulation is presented in section 3.1. A review of wind noise models from literature is presented in section 3.2 considering the models as hypothetical forcing functions on the acoustic production system. For each reviewed literature model, a magnitude-based frequency domain model identification is completed to define an equivalent dynamic system for acoustic production mechanisms. The results of these fits are given in section 3.3 with overall discussion presented in section 3.4.

3.1 System Description

In chapter 1, a simplified block diagram was presented and is reintroduced below as figure 3.1. This chapter revisits the formulation of the problem with emphasis placed on the acoustic production block, $\mathbf{A}$, and breaks the block into two substructures - $\mathbf{A}_0$ which describes a model of the energy or pressure spectra associated with supercell characteristics and $\mathbf{A}_1$ which models a transfer function relating the energy cascade structure to the acoustic output of the system. In section 3.2, a set of models are supposed for $\mathbf{A}_0$ which correlate to tornadic wind expectations and magnitude-based frequency response curve fits are utilized to identify candidate model structures for block $\mathbf{A}_1$.

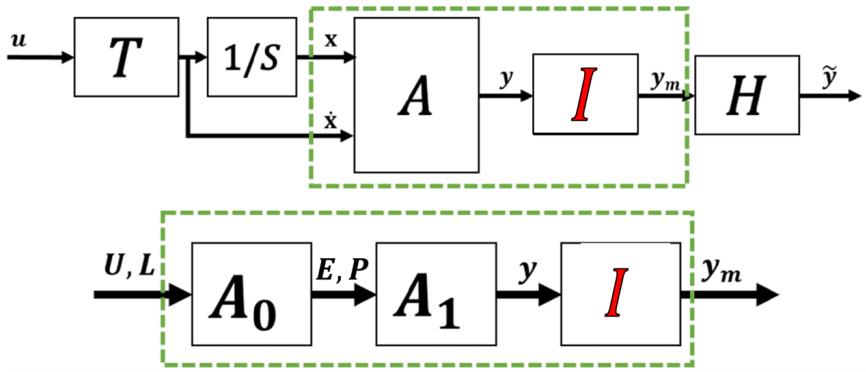

Figure 3.1: Block diagram for tornado acoustics measurement system with acoustic production function broken out

In 1922 Richardson [50] quipped of turbulence, "Big whorls have little whorls Which feed on their velocity, and little whorls have lesser whorls and so on to viscosity." The transfer of energy from large scales of motion to small scales in turbulent flows is described generally by an energy cascade based on physical scaling properties of the flow where the energy transfer is predominantly local in between fluctuations of nearly the same size [46]. Kolmogorov [28] dimensionally defined a scaling factor, η, as function of fluid kinematic viscosity, v and dissipation rate of energy, ϵ (equation3.1) which scale wavenumbers for the energy cascade. The dissipation rate of energy can be described as a proportional relationship between characteristic length, L, and characteristic velocity, U, as in equation 3.2. Results have been shown over the range 0.08 - 0.33 [12; 19; 46; 55] the constant C_ϵ in equation 3.2. The values U and L are examined on order of magnitude, therefore a nominal value of $C_\epsilon = 0.1$ within this range is used for calculation.

$$\eta = (\frac{v^3}{\epsilon})^{1/4} \tag{3.1}$$

$$\epsilon = C_\epsilon \frac{U^3}{L} \tag{3.2}$$

A classical depiction for the energy cascade is presented in figure 3.2. For the energy cascade, there are three primary regions of interest - the integral scale, the

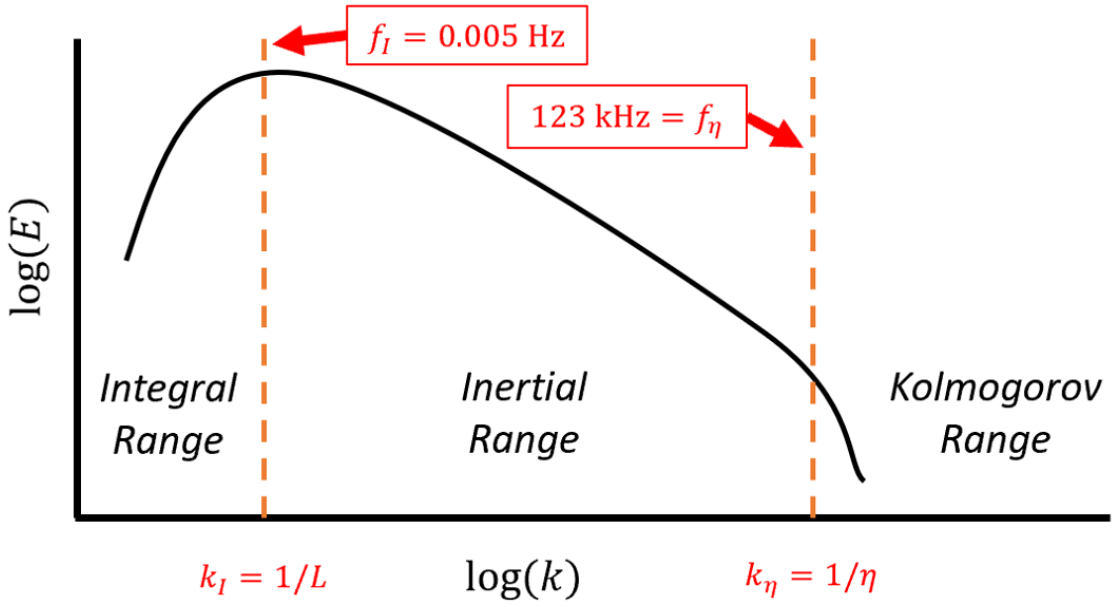

Figure 3.2: Annotated energy cascade diagram for atmospheric parameters during tornadic events

inertial scale, and the Kolmogorov scale which correspond to energy producing eddies, energy transfering eddies, and energy dissipating eddies respectively. The inertial scale is defined by a nearly constant slope over the associated wavenumbers as energy is transfered to smaller eddies. Scaling wavenumber by the Kolmogorov scale, the inertial range is upwardly-bounded by wavenumber $k_\eta = 1/\eta$ where viscosity becomes more significant and dissipation occurs over these eddies [28]. The lower bound for the inertial range is not universally defined, as it is a function of Reynolds number, however, it can be well-approximated as $k_I = 1/L$ [46].

A characteristic length scale $L \geq 10$ km and velocities in excess of $U = 20$ m/s are associated with supercell storm structure and maximum tangential velocity flow field values [27; 54].

These values are used in determining a relevant k_I and k_η for the tornado infrasound structure. The resulting wavenumbers can then be transformed to frequency domain representations f_I and f_η respectively from the definition of wavenumber as defined in equation 3.3, where $c = 343$ m/s nominally is the speed of sound. This

returns $f_I = 0.005$ Hz and $f_\eta = 123$ kHz (Fig 3.2). Because the expected frequencies of tornadic infrasound are around 10 Hz, it can be seen by comparison to the bounds that interest lies in the inertial range exclusively by nearly two frequency decades above and below.

$$f = \frac{kc}{2\pi} \tag{3.3}$$

In the following sections, a tornadic supercell storm system is considered from literature corresponding to the above values. As can be seen in figures 3.2 and 3.4, over the inertial range, forcing models have decaying amplitude with frequency which impacts how many resulting identified fits are proper with respect to transfer function order. Over the integral range, amplitude increases with frequency up to the limit f_I. Over the analysis region [1, 100] Hz, solving the bounding frequency again as $k_I = 1/L$ and converting to frequency as equation 3.3 returns the minimum necessary characteristic length for $f_I \geq 1$ Hz as $L_{1Hz} \leq 55$ m. For the integral range to approach the frequencies associated with tornado infrasound as measured by the GLINDA unit ($f_I \geq 10$ Hz) , the required length changes to $L_{10Hz} \leq 5$ m. The recorded tornado returned an estimated diameter of 137 m at maximum which is well over these required diameters.

3.2 Selected Input Structures

In this section, a set of energy and pressure

3.2.1 White Noise Input

White, Gaussian noise (WGN) is defined as a signal with constant autospectral density and can be considered to have uniform magnitude across all frequencies represented as equation3.4 [45]. As such, the relation between inputs and outputs can be simplified as equation3.5. Recall section 2.4.3 where a transfer function model was

previously curve fit directly to the tornado event acoustics measured by the GLINDA system. This curve fit can additionally be considered the result for $\mathbf{A_1}$ with the assumption of a white noise input spectrum and equation3.5.

$$A_{0,WGN}(f) = 1 \tag{3.4}$$

$$\frac{Y(f)}{X(f)} = \mathbf{A_1}\cancel{\mathbf{A_0}}^{1} = \mathbf{A_1} \tag{3.5}$$

3.2.2 $-5/3$ Power Law

The 1941 Kolmogorov analysis described previously also identified that within the inertial range that kinematic viscosity is largely negligible [28; 29]. For this to be possible, the wavenumber must be raised to the -5/3 power by dimensional analysis. For decades since this was proposed, experimental data has supported this hypothesis [46]. It then follows through his analysis that eddies between the energy producing scale (k_I) and energy dissipating scale (k_η) must scale with a -5/3 power law for the turbulence's energy distribution [28; 29].

Effectively, Kolmogorov's hypotheses stated that the distribution of energy, E, within the fluid follows a somewhat simple formula of wavenumber, characteristic length, and characteristic velocity as described by equation 3.6. Here, $C_{5/3}$ is a constant which has been approximated as 1.6 [25; 66; 67]. Ortiz-Suslow and Wang comments of the -5/3 power law, "Since it was proposed, this theory has formed the basis by which we conceptualize and study fluid turbulence. In the atmosphere, this 5/3 power law is used to study the fundamental physics underlying some of our most pressing problems: forecasting storm intensity, climate-regulating atmosphere-ocean exchange, and ocean wave growth." [40] This model is considered valid over the inertial range although loses accuracy exponentially beginning around $k\eta = 0.2$

(24.6 kHz for the supercell system) [68].

$$E(k) = C_{5/3}\epsilon^{2/3}k^{-5/3} \tag{3.6}$$

3.2.3 $-7/3$ Power Law

Similar to Kolmogorov's dimensional analysis of energy fluctuations through the velocity field, George et al. [20] alternatively developed spectral models for turbulent pressure fluctuations. This model was created by directly Fourier transforming the integral solution to the Poisson equation. They then showed that the pressure spectrum consists of two source terms - a turbulence-turbulence interaction of the $k^{-7/3}$ over the inertial range and dominates the high-wavenumber region and the mean shear-turbulence interaction that is dominant in the energy-containing range and falls off as $k^{-11/3}$ in the inertial range [20].

Over the inertial range, an additional pressure spectrum equation with a -7/3 power law (equation3.7) is consistent with Kolmogorov's dimensional analysis and previous theoretical models [5; 20]. The -7/3 power law additionally has been validated under sufficiently high Reynolds number conditions by experimental results and simulation [22; 58]. For this equation, $C_{7/3} \approx 8$ is reported [23].

$$P(k) = C_{7/3}\epsilon^{4/3}k^{-7/3} \tag{3.7}$$

3.2.4 $1/f^n$ Models

Audible wind noise has a primary origin in turbulences. Strasberg [56] developed a mathematical description of the measured spectra of wind noise under wind screen tests stating that the logarithmic spectrum level L_{log} of the wind noise signal may be written as equation for frequency, f, characteristic wind speed, U, and wind screen diameter, D.

$$L_{log}(f) = 67 + 63\log_{10}(U) - 33\log_{10}(f) - 23\log_{10}(D) \tag{3.8}$$

The loudness level L_{log} is computed to a reference sound pressure of 20 μPa which Nelke [33] transformed into a linear representation of the sound pressure spectrum given by equation 3.9. This relationship was derived empirically for long-term wind measurements ($\geq$ 60 s) and yields two important proportionality relationships: $P(f) \propto U^{3.15}$ and $P(f) \propto 1/f^{1.65}$ [33].

$$P(f) = \frac{(20 \times 10^{-6})(10^{3.35})(U^{3.15})}{f^{1.65}D^{1.15}} \tag{3.9}$$

Comparing the -5/3 power law and the Nelke model reveals a near-equivalent relationship with frequency content as $-5/3 \approx -1.65$. The 0.01 difference in powers generates less than 1% difference in slope and, over the region of interest, a generally negligible difference in magnitude change. A significant difference between the -5/3 power law and the Nelke model is the lack of inclusion of a term related to characteristic length for the storm system in Nelke's analysis. The roll of velocity is additionally increased in Nelke's model with a nearly 150% higher power.

In a short-term measurement structure ($\leq$ 60 s), Nelke [33] notes that the roll off is not consistent with the original $1/f^{1.65}$ value and suggests that $1/f$ is a better representation for the short term spectra (Fig. 3.3) [33]. More generally, he suggests a family of structures defined by equation3.10 is appropriate. In this chapter, both the $n = 1.65$ and $n = 1$ cases will be examined.

$$P(f) \propto \frac{1}{f^n},\ n > 0 \tag{3.10}$$

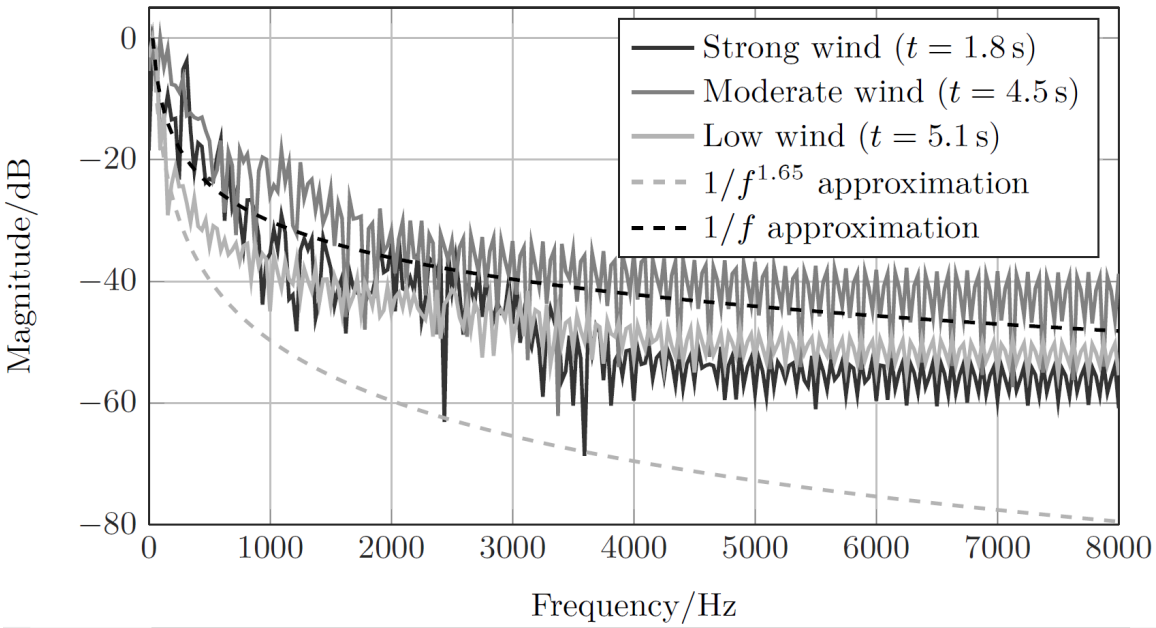

Figure 3.3: Short-term spectra of wind noise segments of different wind intensity. (Adapted from Figure 3.6 - [33])

3.3 Results

This section presents the candidate transfer functions for each of the proposed energy models. For each of the proposed models, transfer functions were obtained via MSE minimization approaches as described in Section 2.4.3. The white noise input case will be considered the base case for comparison in this section.

Fit Name	**Model**	$\mathbf{E_{f_{peak}}}$ (%)	$\mathbf{E_{\lvert H\rvert_{peak}}}$ (%)	**MSE** (dB^2)
$\mathbf{A}_{1,12Z}$	$\dfrac{a_0 b_0 (s+b_1)^2}{(s+a_1)(s^2+b_2 s+b_3)}$	6.6	8.0	1.82
$\mathbf{A}_{1,-5/3}$	$c_0 \dfrac{s(s+c_1)^2}{s^2+c_2 s+c_3}$	2.9	3.7	0.81
$\mathbf{A}_{1,-7/3}$	$c_0 \dfrac{s^2(s+c_1)^2}{s^2+c_2 s+c_3}$	3.9	7.1	1.14
$\mathbf{A}_{1,N165}$	$c_0 \dfrac{s(s+c_1)^2}{s^2+c_2 s+c_3}$	2.4	3.8	0.81
$\mathbf{A}_{1,N100}$	$c_0 \dfrac{(s+c_1)^2}{s^2+c_2 s+c_3}$	12.8	5.8	1.29

Table 3.1: Fit parameters for transfer functions to various wind energy models

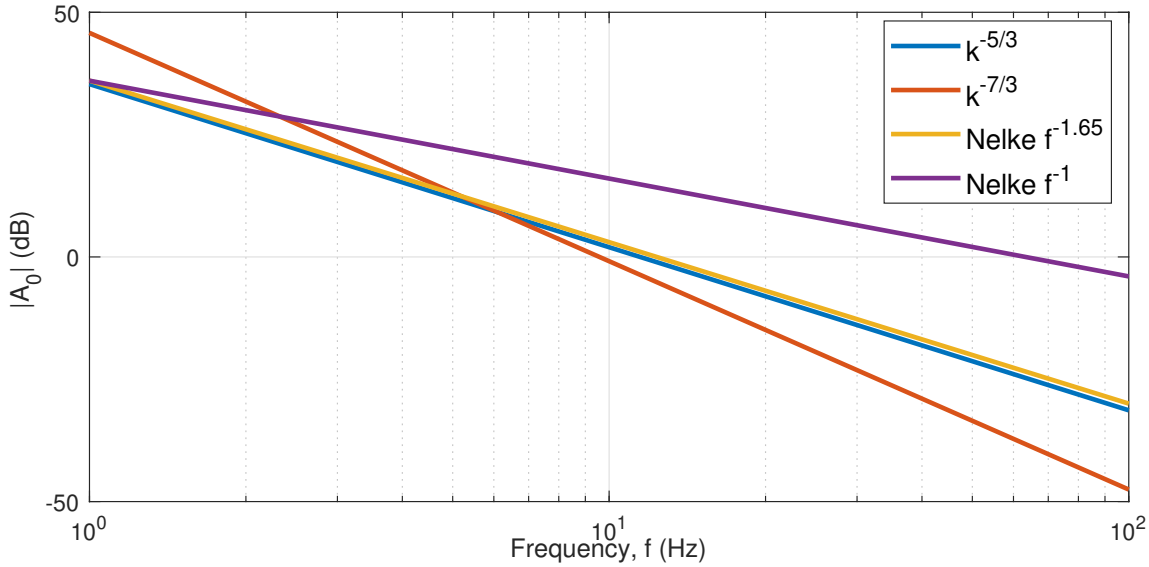

Figure 3.4: Energy spectra associated with wind models over the inertial range for turbulence

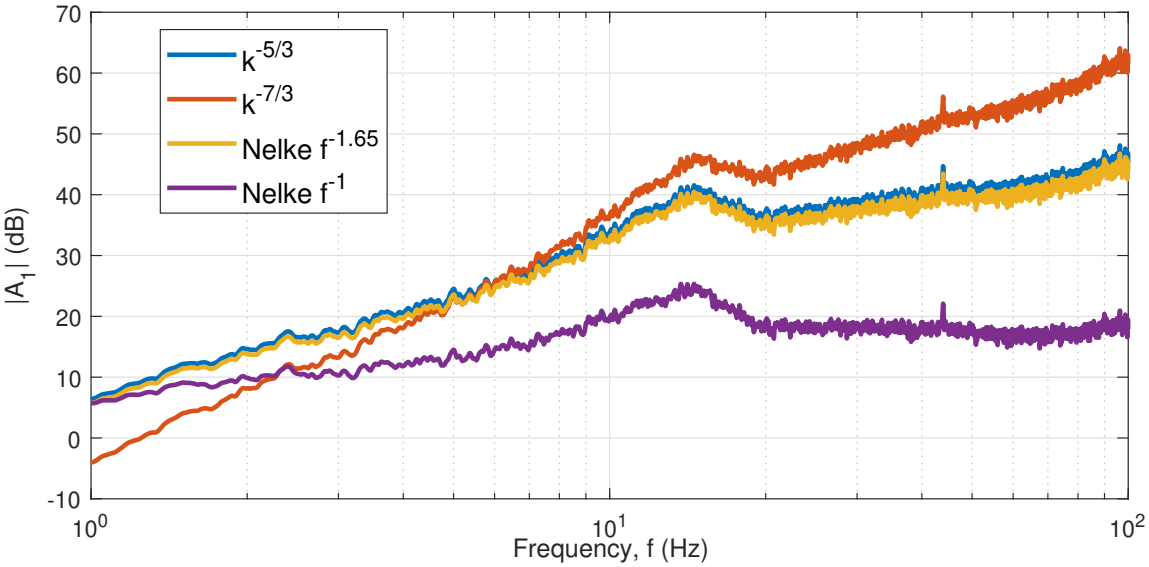

Figure 3.5: Raw frequency response difference between tornado event acoustic spectrum and input energy spectra

3.3.1 White Noise Input

As described in Section 2.4.3, the candidate model which best describes the transfer function for a uniform magnitude input spectrum is provided in equation 3.11 below.

$$\mathbf{A_{1,12Z}} = \left(\frac{1.78 \times 10^5}{s + 25.15}\right)\left(\frac{0.879(s + 72.41)^2}{s^2 + 85.41s + 6266}\right) \tag{3.11}$$

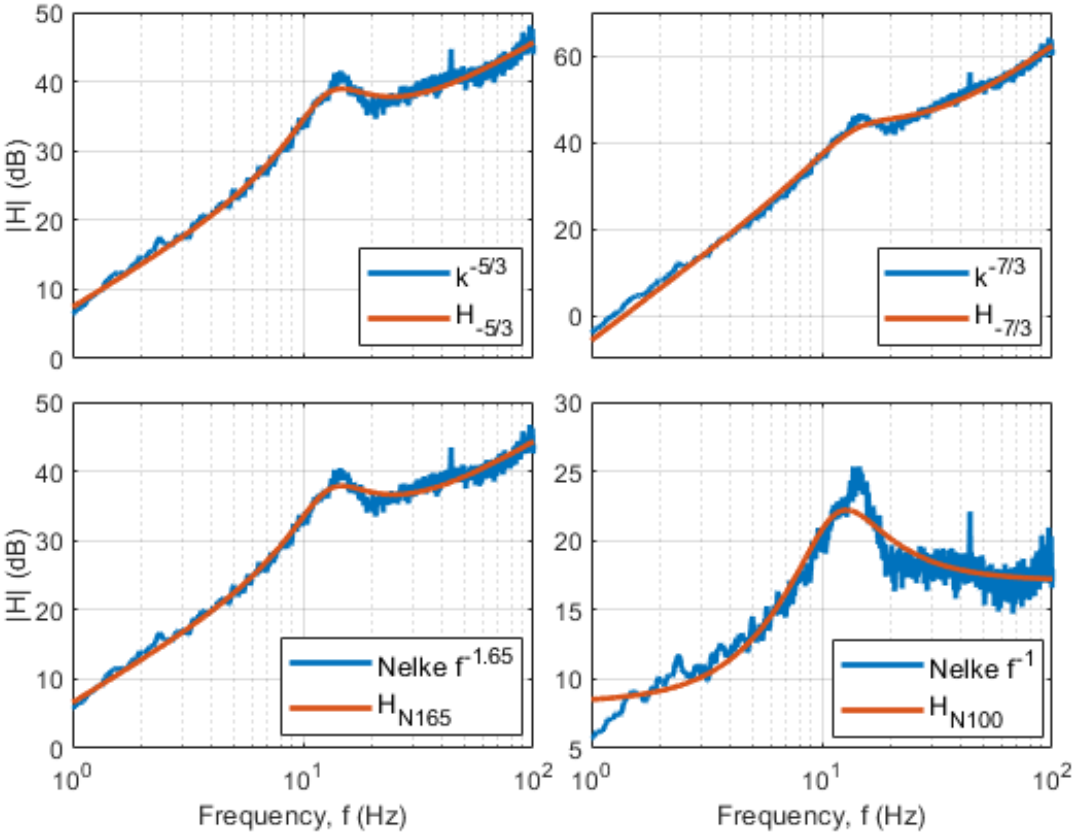

Figure 3.6: Energy spectra associated with wind models over the inertial range for turbulence

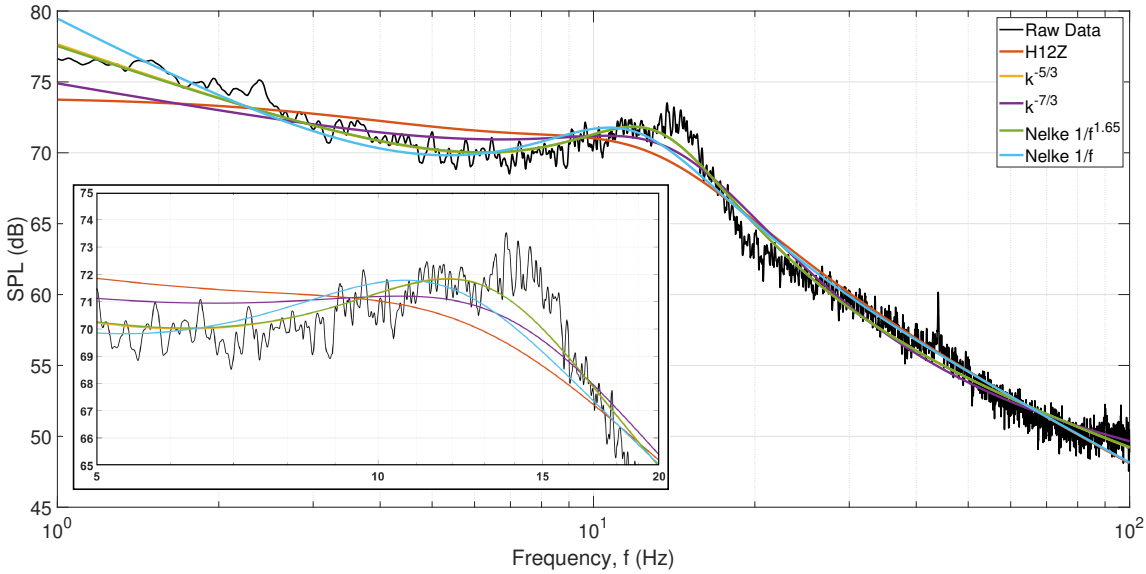

Figure 3.7: Comparison of various wind models and curve fit transfer functions ($\mathbf{A}_0 + \mathbf{A}_1$) overlaid on measured tornado acoustic data

3.3.2 $-5/3$ Power Law

Utilizing the corresponding model structure in table 3.1, a minimum MSE solution is defined by parameters as equation 3.12. Initial parameter guesses for minimization were of order of magnitude anticipated for relevant tornadic infrasound signals. This input/output model structure returns the lowest percent error of peak magnitude among all models while also returning improvements for MSE and percent error of peak frequency as compared to the white noise case.

$$\mathbf{A_{1,-5/3}} = \frac{0.294s(s+92.52)^2}{s^2+53.34s+6790} \tag{3.12}$$

3.3.3 $-7/3$ Power Law

Utilizing the model structure $\mathbf{H}_{-7/3}$ in table 3.1, a minimum MSE solution is given by equation3.13. All minimization initial parameter guesses were of order of magnitude anticipated for relevant tornadic infrasound signals. This model structure returns lower MSE, percent error of peak frequency, and percent error of peak magnitude than the initial white noise case.

$$\mathbf{A_{1,-7/3}} = \frac{0.003s^2(s+182.9)^2}{s^2+76.79s+7768} \tag{3.13}$$

3.3.4 $1/f^n$ Models

For both Nelke wind models, an assumption of $D = 1$ was made as D is an incalculable value from the current data sets. As D is a constant in equation3.9, it plays no difference in the transfer function results besides a uniform offset over all frequencies. There is a significant overlap between the spectral content of the $-5/3$ power law and $n = 1.65$ Nelke model (equation3.14) although the difference of models increases with increased frequency decade. As follows from the $-5/3$ case, this model represents an improvement to the MSE and percent error of peak magnitude as compared to

the white noise case. Additionally this model represents the minimal percent error in peak frequency identification for all models.

$$\mathbf{A_{1,N165}} = \frac{0.252s(s+95.75)^2}{s^2+53.84s+6850} \tag{3.14}$$

Equation 3.15 represents the minimal MSE solution to the Nelke $n = 1$ model structure. This model returns nearly double the percent error for peak frequency compared to the white noise case while only modest improvements to peak magnitude percent error and MSE.

$$\mathbf{A_{1,N100}} = \frac{7.156(s+44.64)^2}{s^2+57.07s+5472} \tag{3.15}$$

3.4 Discussion

In comparison of the set of models, a considerable commonality of structure can be observed. In each of the models, a repeated zero and pair of underdamped complex poles which correspond to the rise associated with the tornadic infrasound signature. Table 3.2 presents the repeated zero, z_r, damping ratio, ζ, and natural frequency, ω_n for each transfer function model. A time constant, τ, was computed via equation 3.16 for each model with values additionally reported in Table 3.2.

Fit Name	z_0 (rad/s)	ζ (-)	ω_n (rad/s)	τ (s/rad)
$\mathbf{A}_{1,12Z}$	71.4	0.539	79.2	0.023
$\mathbf{A}_{1,-5/3}$	92.5	0.324	82.4	0.037
$\mathbf{A}_{1,-7/3}$	182.9	0.436	88.1	0.026
$\mathbf{A}_{1,N165}$	95.8	0.325	82.8	0.037
$\mathbf{A}_{1,N100}$	44.6	0.386	74.0	0.035

Table 3.2: Tornado acoustics associated transfer function characteristics

$$\tau = \frac{1}{\zeta w_n} \tag{3.16}$$

In this thesis, the standard definitions for proper and strictly proper transfer

functions are observed as transfer functions in which the degree of the numerator does not exceed the degree of the denominator and where the degree of the numerator is less than the degree of the denominator respectively. A strictly proper transfer functions will approach zero magnitude as frequency approached infinity, while a proper transfer function can only be guaranteed to never grow unbounded with increasing frequency. It can be seen in Table 3.1, the only strictly proper transfer function result is $\mathbf{A}_{1,12Z}$. $\mathbf{A}_{1,N100}$ is the only proper transfer function. Neither of these models would diverge to infinite magnitude with increasing frequency. The remaining models ($\mathbf{A}_{1,N165}$, $\mathbf{A}_{1,-5/3}$, and $\mathbf{A}_{1,-7/3}$) are left as not proper. In physical reasoning, however, the energy and pressure inputs used to derive the associated models do not contain energy at infinite (or sufficiently large) frequencies. As seen in figure 3.2, energy dissipates at high frequencies due to viscous effects and decays to zero with increasing frequency and prevents unbounded response by these models.

A physical system generally must satisfy being strictly proper with negative slope after some break frequency for the system, ω_b. Because measurements for the system's acoustic transfer functions are made over the limited interval of infrasound and low-auditory frequencies between 1 and 100 Hz, the apparent proper transfer function may be strictly proper under an expanded frequency interval as exampled in Figure 3.8.

A consideration hereto unaddressed has been the impact of the vehicle to the acoustic measurements. Recall the measurement device associated block, $\mathbf{H}$, from the problem construction given in figure 1.3. Note that this block can be expanded as Figure 3.9 where $\mathbf{H}_{u/d}$ refers to the truck acoustic transfer function based on window configuration and $\mathbf{H}_m$ is the transfer function of the microphone response as represented in Figure 2.1. To resolve the lack of inclusion for the truck effect on the acoustic measurements, a transfer function is defined $\mathbf{A}'_{1,*} = \mathbf{A}_{1,*}\mathbf{H}_u^{-1}$ where $\mathbf{H}_u$ is described in section 2.4.1 as the transfer function associated with acoustic propagation

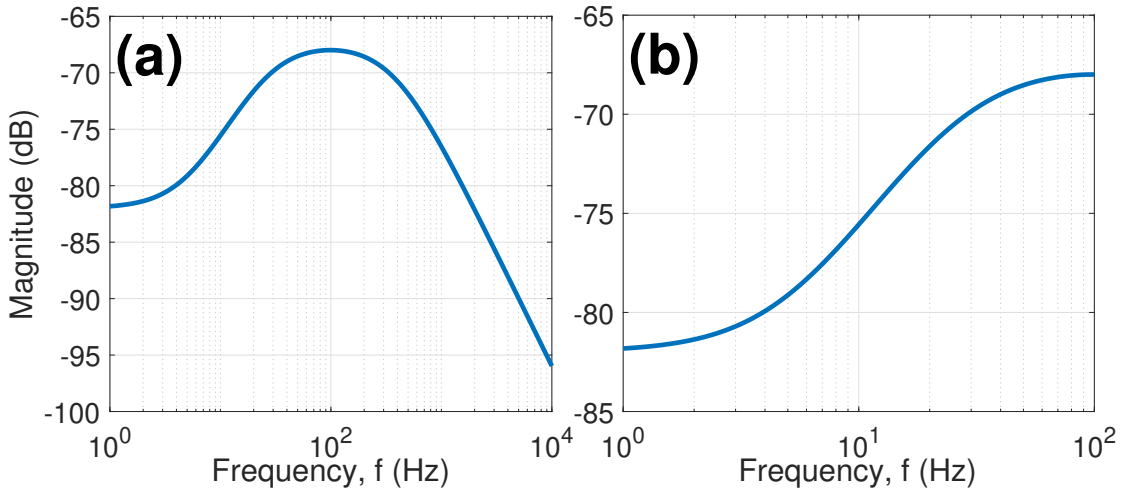

Figure 3.8: Example transfer function, $H_e = (s+10\pi)/(s^2+800\pi s+(200\pi)^2$, viewed over frequency bands containing ω_b (a) and ending prior to the break frequency (b)

through the windows up configuration of the storm chasing vehicle. The coefficients for the various $\mathbf{A}'_{1,*}$ models are provided in Table 3.3.

Because $\mathbf{H}_u$ is a proper transfer function over the region of interest, the inclusion of this term in $\mathbf{A}'_{1,*}$ does not impact the classifications of the previous paragraph established by $\mathbf{A}_{1,*}$.

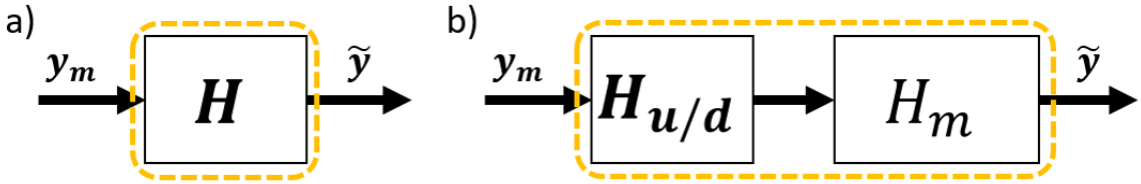

Figure 3.9: The measurement block in (a) is composed of the truck frequency response, $H_{u/d}$, and microphone response, H_m (provided in figure 2.1), as in (b)

By transforming the transfer function $\mathbf{A}'_{1,12Z}$ to state space form via equation 3.17, a set of matrices fitting the structure of equation 3.18 with parameters given in equations 3.19 - **??**. The contextualization of the model in canonical form may yield additional insight to the model structure through comparison to representative systems.

$$H = C(sI - A)^{-1}B + D \tag{3.17}$$

Fit	Num/Den	s^6	s^5	s^4	s^3	s^2	s^1	s^0
$A'_{1,12Z}$	$\mathcal{N}$	-	-	1.56×10^{5}	1.40×10^{8}	3.99×10^{10}	3.80×10^{12}	1.15×10^{14}
	$\mathcal{D}$	-	0.22	38.18	3602	1.75×10^{5}	4.02×10^{6}	3.44×10^{7}
$A'_{1,-5/3}$	$\mathcal{N}$	-	0.294	276.1	8.53×10^{4}	9.63×10^{6}	3.58×10^{8}	0
	$\mathcal{D}$	-	-	0.22	25.59	2.45×10^{3}	1.06×10^{5}	1.48×10^{6}
$A'_{1,-7/3}$	$\mathcal{N}$	0.003	3.36	1.35×10^{3}	2.32×10^{5}	1.43×10^{7}	0	0
	$\mathcal{D}$	-	-	0.22	30.75	2.99×10^{3}	1.24×10^{5}	1.70×10^{6}
$A'_{1,N165}$	$\mathcal{N}$	-	0.252	238.3	7.45×10^{4}	8.60×10^{6}	3.28×10^{8}	0
	$\mathcal{D}$	-	-	0.22	25.7	2.47×10^{3}	1.07×10^{5}	1.50×10^{6}
$A'_{1,N100}$	$\mathcal{N}$	-	-	7.16	6.04×10^{3}	1.51×10^{6}	1.02×10^{8}	2.03×10^{9}
	$\mathcal{D}$	-	-	0.22	26.42	2.21×10^{3}	8.83×10^{4}	1.20×10^{6}

Table 3.3: Coefficients for transfer functions $A'_{1,*}$ which include the calibration acoustic transfer function for the storm chasing truck

$$\begin{aligned} \dot{x} &= Ax + Bu \\ y &= Cx \end{aligned} \tag{3.18}$$

$$A = \begin{bmatrix} -173.5 & -1.64 \times 10^4 & -7.97 \times 10^5 & -1.83 \times 10^7 & -1.56 \times 10^8 \\ 1 & 0 & 0 & 0 & 0 \\ 0 & 1 & 0 & 0 & 0 \\ 0 & 0 & 1 & 0 & 0 \\ 0 & 0 & 0 & 1 & 0 \end{bmatrix} \tag{3.19}$$

$$B = \begin{bmatrix} 1 & 0 & 0 & 0 & 0 \end{bmatrix}^T \tag{3.20}$$

$$C = \begin{bmatrix} 7.09 \times 10^5 & 6.37 \times 10^8 & 1.81 \times 10^{11} & 1.73 \times 10^{13} & 5.22 \times 10^{14} \end{bmatrix} \tag{3.21}$$

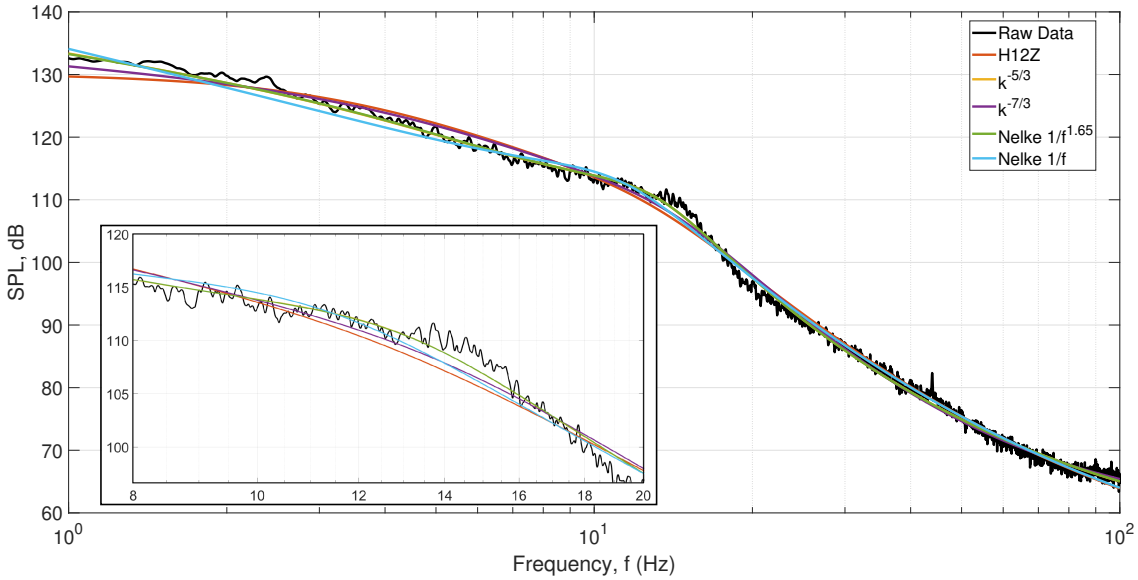

Figure 3.10: Measurements and overlaid curve fit models with calibration estimation included ($Y = A_0 A_1'$)

CHAPTER IV

Conclusion and Future Work

4.1 Conclusions

Sparse tornadic infrasound measurements have limited their application in predictive work. To improve the availability and quality of observations of infrasound from tornadoes, a ground-based infrasound data acquisition system (termed GLINDA) that includes an infrasound microphone, an IMU, and a GPS receiver has been designed and deployed. The infrasound microphone has sensitivity of 0.401 V/Pa with a flat (to -3 dB) response from 0.1 to 200 Hz and the 36 V peak-to-peak analog output is sampled at 2050 Hz via ADC to mitigate aliasing of signals with significant magnitude. This microphone, voltage divider circuit, and ADC measurement path maintains resolution of 1.4 mPa which sets the quantization error below existing noise floor estimates from existing array measurements at 20 mPa. The GLINDA system operates on a Raspberry Pi 3B+ platform with the data exported to an online repository and processed for realtime display of spectra and model fitting in an online display portal with update rates similar to radar. The processing tools incorporate the Chirp Z transform and windowing to reduce the uncertainty of the signal, as verified by a 50% reduction in standard deviation.

GLINDA was installed in a storm chasing vehicle and has been acquiring data from May 2020 to present. It has recorded several severe weather events, including a dust storm, gustnado, fires, and significant hail. This paper provides design details and analysis from two events - a tornado and a significant hail storm. The tornado occurred in the early hours of 22 May 2020 near Lakin, KS. The tornado lasted 13

minutes, had a length of 2.8 km, and a maximum damage path width of 137 m, and unknown strength. The storm chasers measured this system from 4 km SSE of the tornado. The spectral content shows an elevated signal during the tornado spanning 10 to 15 Hz, consistent with past observations of small tornadoes. The hail event occurred the following evening at 2315 UTC on 22 May 2020 with 25.4 mm hail while the storm chasers were located in Oklahoma's Comanche County. Similar spectral analysis was performed on this event but no significant infrasound production was identified relative to periods before and after the hail.

These results indicate consistency of the mobile observations with fixed measurements and support this modality as a means of increasing the availability and signal to noise ratio of tornado infrasound observations, and the analysis shows an improvement in precision enabled my real-time model-fitting based processing tools to resolve and quantify spectral deviations associated with tornado activity.

By taking order of magnitude estimates for characteristic length and wind speed associated with acoustic production in tornadic structures an energy cascade diagram was characterized. This diagram shows that all frequencies associated with tornadic infrasound are located in the inertial range and nearly two decades removed from both the integral and Kolmogorov ranges.

Utilizing a series of wind models to define input energy spectra, a series of frequency response curve fits were made as transfer functions between energy and sound pressure level. Among the models tested, a curve fit with minimal percent error on peak magnitude was completed for input spectra associated with the conventional $-5/3$ power law observed in the inertial range of the energy cascade model. A similar percent error on peak magnitude can be observed in the curve fit to the Nelke $1/f^{1.65}$, however, this frequency response curve fit exhibits a notably smaller percent error on peak frequency.

Only one model returned through magnitude-based system identification of trans-

fer functions is strictly proper, however, the limited frequency window of analysis may obscure features including break frequency beyond this window. Therefore, these models cannot be entirely discounted solely on their classification of properness.

4.2 Limitations and Future Works

Perhaps the most significant limitation of this work is the analysis of a singular event. With regard to GLINDA measurement opportunities, over the last eighty years, a thirteen month period in Oklahoma spanning the time frame of GLINDA's deployment (May through May of the next year) has an average of 82 tornadoes. During the course of this thesis study and deployment of the GLINDA unit, Oklahoma has experienced only 36 tornadoes which represents a generally low-tornadic period for the state at large. The lower number of tornadoes has notably decreased the likelihood of the already difficult measurement problem presented and therefore returned notably less measured tornadoes than in a span of time closer to the mean of tornadoes might.

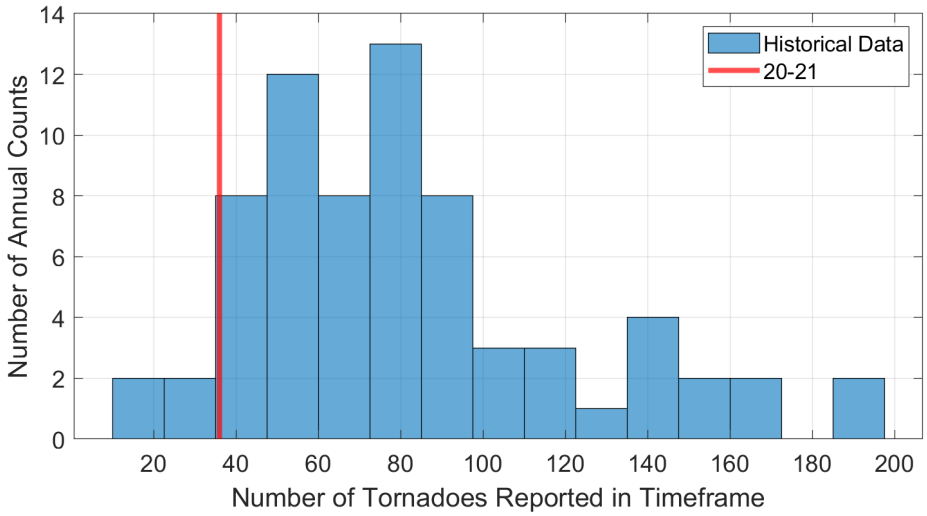

Figure 4.1: Comparison of May 2020 - May 2021 reported Oklahoma tornadoes and historical records for reported tornadoes over time period May 01 - May 31 of the next year since 1950

Attempting to use similar analysis as presented for GLINDA's measurements on the infrasound array (IA1) located on Oklahoma State University's campus (described

in Elbing et al. [16]) faces significant difficulties. As can be seen in figure 4.2, the measured signal during the tornado reaches and trails off with the noise floor at just over 20 Hz. Because the noise floor for this system is flat over the frequency band 20 - 80 Hz, a roll off in magnitude similar to the spectra in figure 2.12 cannot be observed. The noise floor additionally prevents convergence of the models presented in chapter 2 due to a peak at approximately 50 Hz which is consistent between calm and storm measurements on the IA1 system.

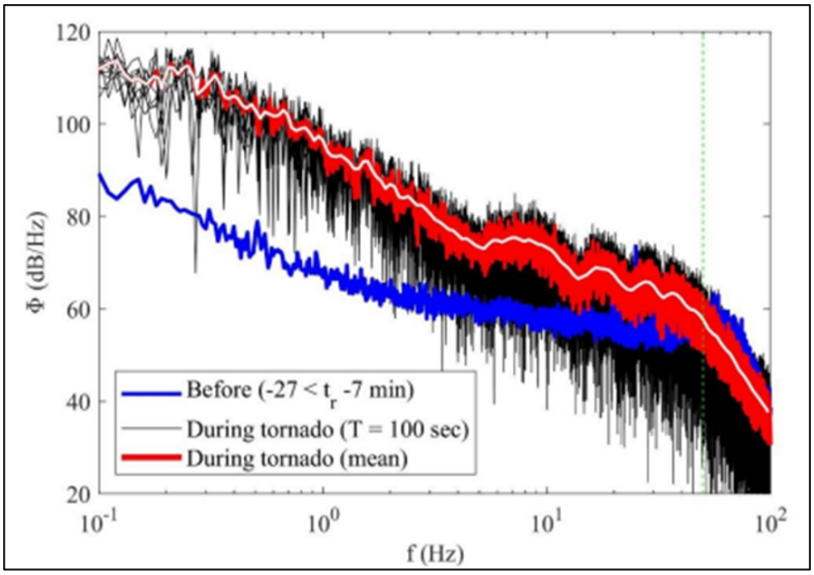

Figure 4.2: IA1-measured tornado spectra and static measurements prior to tornadogenesis as reported in figure 8, Elbing et al. [16]

While GLINDA represents a mobile and flexible platform for infrasound measurement, it is still only singular source of collecting data. While it is expected (and empirically shown) to increase the number of samples available for study, further work in this area would expand the number of GLINDA units in operation. This would likely dramatically increase coverage area of tornado acoustic awareness and sampling capabilities. Such manufactured units are a continuing work, but are not expanded upon in detail as they are not included in this thesis as presented. To improve the uncertainty around this measurement and the associated models, the collection of additional tornado infrasound samples is necessary through GLINDA,

future iterations of mobile sensors, and existing tornado infrasound systems to allow for independent and cross-verified signal measurements. The inclusion of additional data sets additionally will allow for more robust modelling procedures which can be compared to hypothesized infrasound production models such as presented in section 1.2.2.3.

The collection of additional data would allow for statistical evaluation of model fit parameters to provide more certainty to the analysis.

A final area of future work is to use infrasound detection capabilities to simulate local flow fields in near real-time. Abdullah's 1966 analysis [1] presents an algebraic relationship between fundamental frequency of tornadic infrasound and core width. Bedard [6] later noted that the first harmonic of the frequency observed by Abdullah provided a better fit to observations. Ash et al. [3] solved an acoustic-producing formulation of the Navier-Stokes equation for tangential velocity as a function of only, core radius, the empirically obtained value η_p describing the constant volume (density) relaxation time, and kinematic viscosity of the surrounding air. Combining these two approaches allows for an estimate of the flow field and circulation aboud the source of an identified tornadic fundamental frequency (figure 4.3). With further acoustic data collection and local atmospheric measurements, these models could be tested and validated in further work.

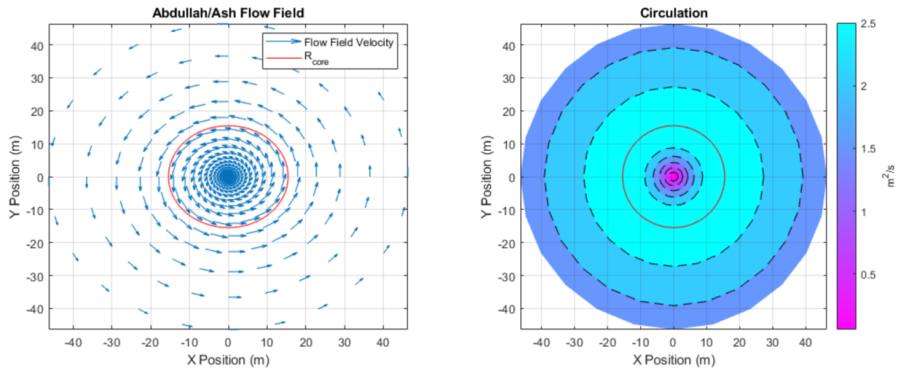

Figure 4.3: Demonstration of flow field and circulation estimation via Abdullah [1] core radius analysis and Ash et al. [3] velocity estimates

References

[1] A. J. Abdullah. The musical sound emitted by a tornado. *Monthly Weather Review*, 94(4):213, 220, 1966.

[2] M. Akhalkatsi and G. Gogoberidze. Spectrum of infrasound radiation from supercell storms. *Quarterly Journal of the Royal Meteorological Society*, 137(654):229–235, 2011.

[3] R. L. Ash and I. R. Zardadkhan. Non-equilibrium behavior of large-scale axial vortex cores. *AIP Advances*, 11(2):025320, 2021.

[4] W. S. Ashley. Spatial and temporal analysis of tornado fatalities in the United States: 1880-2005. *Weather and Forecasting*, 22(6):1214–1228, 2007.

[5] G. K. Batchelor. Pressure fluctuations in isotropic turbulence. *Mathematical Proceedings of the Cambridge Philosophical Society*, 47(2):359–374, 1951.

[6] A. J. Bedard. Low-frequency atmospheric acoustic energy associated with vortices produced by thunderstorms. *Monthly Weather Review*, 133(1):241, 263, 2005.

[7] A. J. Bedard, B. W. Bartram, B. Entwistle, J. Golden, S. Hodanish, R. M. Jones, R. T. Nishiyama, A. N. Keane, L. Mooney, M. Nicholls, E. J. Szoke, E. Thaler, and D. C. Welsh. Overview of the isnet data set and conclusions and recommendations from a march 2004 workshop to review isnet data. In *22nd Conference on Severe Local Storms*, Hyannis, MA, 2004. American Meteorological Society.

[8] A. J. Bedard, B. W. Bartram, A. N. Keane, D. C. Welsh, and R. T. Nishiyama.

The infrasound network (isnet): Background, design details, and display capabilities as an 88d adjunct tornado detection tool. In *22nd Conference on Severe Local Storms*, Hyannis, MA, 2004. American Meteorological Society.

[9] D. C. Bowman, P. E. Norman, M. T. Pauken, S. A. Albert, D. Dexheimer, X. Yang, S. Krishnamoorthy, A. Komjathy, and J. A. Cutts. Multihour stratospheric flights with the heliotrope solar hot-air balloon. *Journal of Atmospheric and Oceanic Technology*, 37(6):1051, 1066, 2020.

[10] C. R. Church, J. T. Snow, and E. M. Agee. Tornado vortex simulation at purdue university. *Bulletin of the American Meteorological Society*, 58(9):900 – 909, 1977.

[11] C. R. Church, J. T. Snow, G. L. Baker, and E. M. Agee. Characteristics of tornado-like vortices as a function of swirl ratio: A laboratory investigation. *Journal of the Atmospheric Sciences*, 36(9):1755–1776, 1979.

[12] B. Cushman-Roisin and J.-M. Beckers. *Introduction to geophysical fluid dynamics physical and numerical aspects*. Academic Press, 2011.

[13] C. J. R. C. S. S. M. M. Daniel, A.E. New wsr-88d operational techniques: Responding to recent weather events, 2014.

[14] R. P. Davies-Jones. Tornado dynamics. *Thunderstorm morphology and dynamics*, 2:197–236, 1986.

[15] R. W. Dunn, J. A. Meredith, A. B. Lamb, and E. G. Kessler. Detection of atmospheric infrasound with a ring laser interferometer. *Journal of Applied Physics*, 120(12):123109, 2016.

[16] B. R. Elbing, C. E. Petrin, and M. S. Van Den Broeke. Measurement and characterization of infrasound from a tornado producing storm. *Journal of the Acoustical Society of America*, 146(3):1528, 1540, 2019.

[17] B. H. Fiedler. On modelling tornadoes in isolation from the parent storm. *Atmosphere-Ocean*, 33(3):501–512, 1995.

[18] W. G. Frazier, C. Talmadge, J. Park, R. Waxler, and J. Assink. Acoustic detection, tracking, and characterization of three tornadoes. *Journal of the Acoustical Society of America*, 135(4):1742, 1751, 2014.

[19] C. Friehe, C. W. Atta, and C. Gibson. Jet turbulence dissipation rate measurements and correlations. 1971.

[20] W. K. George, P. D. Beuther, and R. E. A. Arndt. Pressure spectra in turbulent free shear flows. *Journal of Fluid Mechanics*, 148:155–191, 1984.

[21] T. M. Georges. Infrasound from convective storms: Examining the evidence. *Reviews of Geophysics*, 11(3):571, 594, 1973.

[22] T. Gotoh and D. Fukayama. Pressure spectrum in homogeneous turbulence. *Physical Review Letters*, 86(17):3775–3778, 2001.

[23] T. Gotoh and D. Fukayama. Pressure spectrum in homogeneous turbulence. *Phys. Rev. Lett.*, 86:3775–3778, Apr 2001.

[24] B. Goudeau, K. R. Knupp, W. G. Frazier, R. Waxler, C. Talmadge, and C. Hetzer. An analysis of tornado-emitted infrasound during the vortex-se field campaign. In *19th Symposium on Meteorological Observation and Instrumentation*, volume 11.6 of *Field Projects I*, Austin, Texas, 2018. American Meteorological Society.

[25] U. Högström. Review of some basic characteristics of the atmospheric surface layer. *Boundary-Layer Meteorology 25th Anniversary Volume, 1970–1995*, page 215–246, 1996.

[26] C. D. Karstens, T. M. Samaras, B. D. Lee, W. A. Gallus, and C. A. Finley. Near-ground pressure and wind measurements in tornadoes*. *Monthly Weather Review*, 138(7):2570–2588, 2010.

[27] J. B. Klemp. Dynamics of tornadic thunderstorms. *Annual Review of Fluid Mechanics*, 19(1):369–402, 1987.

[28] A. N. Kolmogorov. Dissipation of energy in locally isotropic turbulence. *Comptes Rendus de l'Acadamie Des Sciences de l'U.R.S.S.*

[29] A. N. Kolmogorov. The local structure of turbulence in incompressible viscous fluid for very large reynolds numbers. *Doklady Akademii Nauk SSSR.*

[30] W. S. Lewellen, D. C. Lewellen, and R. I. Sykes. Large-eddy simulation of a tornado's interaction with the surface., 1997.

[31] I. Lin, Y.-R. Hsieh, P.-F. Shieh, H.-C. Chuang, L.-C. Chou, et al. The effect of wind on low frequency noise. In *INTER-NOISE and NOISE-CON Congress and Conference Proceedings*, volume 249, pages 1137–1148. Institute of Noise Control Engineering, 2014.

[32] C. Nelke, P. Jax, and P. Vary. Wind noise detection: Signal processing concepts for speech communication. *Energy*, 60(40):20, 2016.

[33] C. M. Nelke. *Wind noise reduction: signal processing concepts.* PhD thesis, 2016.

[34] C. M. Nelke, N. Chatlani, C. Beaugeant, and P. Vary. Single microphone wind noise psd estimation using signal centroids. In *2014 IEEE International Conference on Acoustics, Speech and Signal Processing (ICASSP)*, pages 7063–7067, 2014.

[35] NOAA. Ncei storm event database: Kansas/kearny co./may 21, 2020/tornado, 2020.

[36] NOAA. Ncei storm event database: Oklahoma/comanche co./may 22, 2020/hail, 2020.

[37] NOAA. Tornadoes - annual 2019, Jan 2020.

[38] NOAA/SPC. Noaa/nws storm prediction center, 2021.

[39] J. M. Noble and S. M. Tenney. Detection of naturally occurring events from small aperture infrasound arrays. In *The Battlespace Atmospheric and Cloud Impacts on Military Operations Conference*, Monterey, CA, 2003.

[40] D. G. Ortiz-Suslow and Q. Wang. An evaluation of kolmogorovs 5/3 power law observed within the turbulent airflow above the ocean. *Geophysical Research Letters*, 46(24):14901–14911, 2019.

[41] B. K. Paul and M. Stimers. Exploring probable reasons for record fatalities: The case of 2011 Joplin, Missouri, Tornado. *Natural Hazards*, 64(2):1511–1526, 2012.

[42] C. Petrin, R. KC, and B. R. Elbing. Deployment of a mobile four sensor infrasound array for severe weather. In *73rd Annual Meeting of the APS Division of Fluid Dynamics*, volume E02.01, Chicao, IL (virtual), 2020. American Physical Society.

[43] C. E. Petrin and B. R. Elbing. Infrasound emissions from tornadoes and severe storms compared to potential tornadic generation mechanisms. *Proceedings of Meetings on Acoustics*, 36(1):045005, 2019.

[44] C. E. Petrin and B. R. Elbing. Infrasound emissions from tornadoes and severe storms compared to potential tornadic generation mechanisms. In *Proceedings of Meetings on Acoustics*, page 045005. Acoustical Society of America, 2019.

[45] A. G. Piersol and J. S. Bendat. *Random data: analysis and measurement procedures*. Wiley, 2013.

[46] S. B. Pope. *Turbulent flows*. Cambridge University Press, 2000.

[47] J. E. Prassner and J. M. Noble. Acoustic energy measured from mesocyclone and tornadoes in june 2003. In *The 22nd Conference on Severe Local Storms*, volume 1.3, Hyannis, MA, 2004. American Meteorological Society.

[48] L. R. Rabiner, R. W. Schafer, and C. M. Rader. Chirp z-transform algorithm. *IEEE Transactions on Audio and Electroacoustics, vol. 17, no. 2, pp. 86-92*, June 1969.

[49] M. Refan and H. Hangan. Near surface experimental exploration of tornado vortices. *Journal of Wind Engineering and Industrial Aerodynamics*, 175:120–135, 2018.

[50] L. F. Richardson. *Weather prediction by numerical process*. University Press, 1922.

[51] H. S. Rinehart. Application of a blind source separation algorithm for the detection and tracking of tornado-generated infrasound emissions during the severe weather outbreak of 27 april 2011. *Journal of the Acoustical Society of America*, 132(3):2074, 2012.

[52] H. S. Rinehart. Direct detection of tornadoes using infrasound remote sensing: Assessment of capabilities through comparison with dual polarization radar and other direct detection measurements, 2018.

[53] A. Ross, J. Jacob, and A. Arena. Continued design and development of a tornado intercept unmanned aerial vehicle. 06 2020.

[54] R. Rotunno. The fluid dynamics of tornadoes. *Annual Review of Fluid Mechanics*, 45(1):59–84, 2013.

[55] K. R. Sreenivasan. On the universality of the kolmogorov constant. *Physics of Fluids*, 7(11):2778–2784, 1995.

[56] M. Strasberg. Dimensional analysis of windscreen noise. *The Journal of the Acoustical Society of America*, 83(2):544–548, 1988.

[57] M. B. Tischler and R. K. Remple. *Aircraft and rotorcraft system identification: engineering methods with flight-test examples*. American Institute of Aeronautics and Astronautics, 2012.

[58] Y. Tsuji and T. Ishihara. Similarity scaling of pressure fluctuation in turbulence. *Physical Review E*, 68(2), 2003.

[59] N. US Department of Commerce, Mar 2017.

[60] N. US Department of Commerce, Apr 2019.

[61] US-NWS.

[62] A. Vance, J. Jacob, and B. R. Elbing. Preliminary observations from high altitude solar balloons. In *AGU Fall Meeting*, volume P050-10, virtual, 2020. American Geophysical Union.

[63] N. B. Ward. The exploration of certain features of tornado dynamics using a laboratory model. *Journal of the Atmospheric Sciences*, 29(6):1194–1204, 1972.

[64] B. White, C. Petrin, I. Faruque, and B. Elbing. System identification approaches to modeling of tornado acoustic mechanisms. *Bulletin of the American Physical Society*, 2020.

[65] W. P. Winn, S. J. Hunyady, and G. D. Aulich. Pressure at the ground in a large tornado., 1999.

[66] A. M. YAGLOM. Laws of small scale turbulence in atmosphere and ocean (in commemoration of the 40th anniversary of the theory of locally isotropic turbulence). *Izv. Atmos. Oceanic Phys.*, 17:1235–1257, 1981.

[67] P. K. Yeung and Y. Zhou. Universality of the kolmogorov constant in numerical simulations of turbulence. *Physical Review E*, 56(2):1746–1752, 1997.

[68] S. Zhao, M. Dabin, E. Cheng, X. Qiu, I. Burnett, and J. C.-C. Liu. On the wind noise reduction mechanism of porous microphone windscreens. *The Journal of the Acoustical Society of America*, 142(4):2454–2463, 2017.

APPENDIX A

GLINDA Images and Wiring

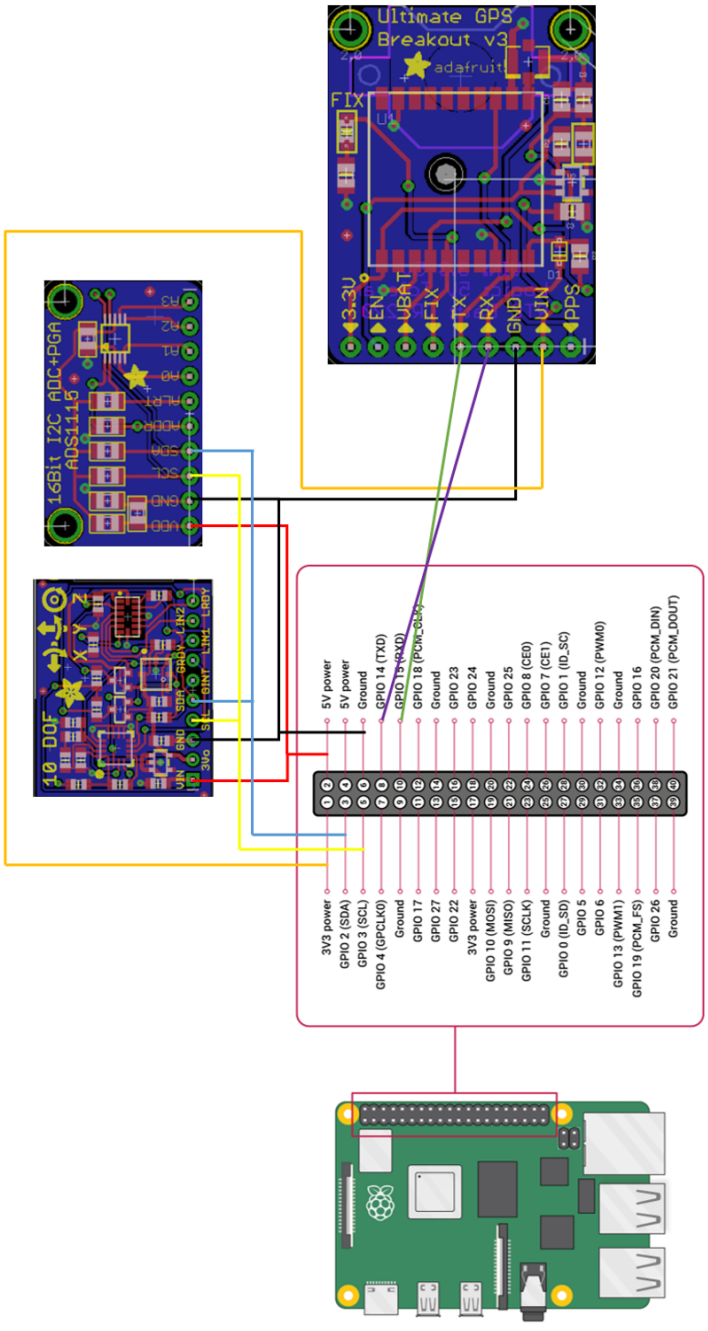

Figure A.1: GLINDA Wiring diagram

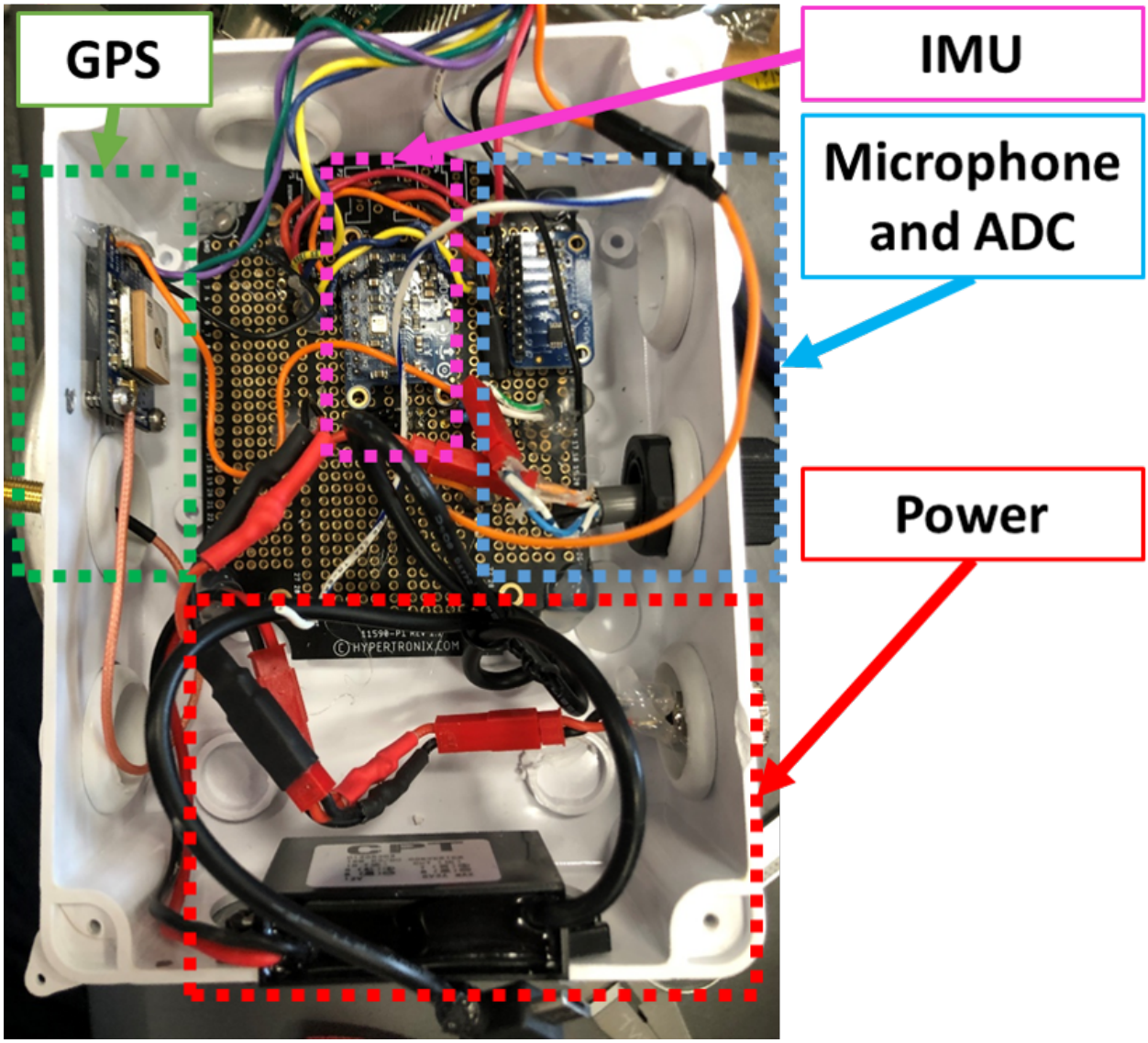

Figure A.2: GLINDA Layout

APPENDIX B

GLINDA System Static Measurement

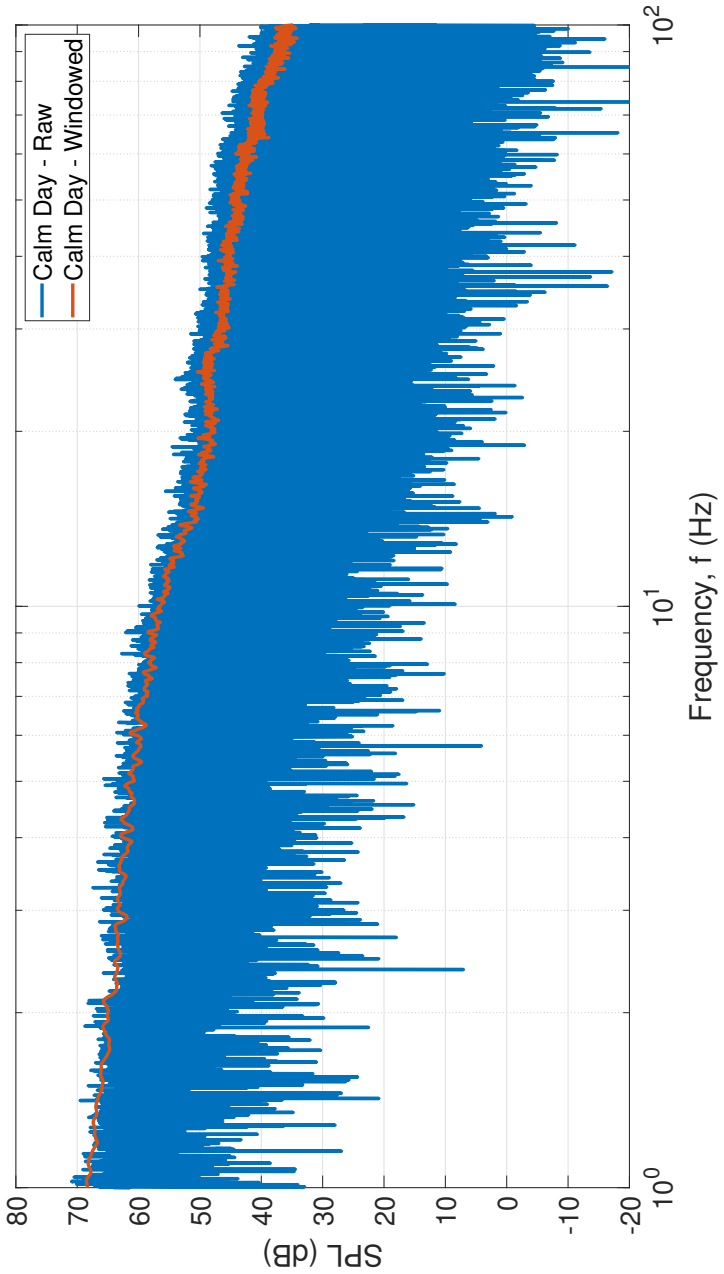

Figure B.1: GLINDA acoustic measurements during calm weather day as raw and windowed per section 2.2.2

VITA

Brandon C. White

Candidate for the Degree of

Masters of Science

Thesis: MEASUREMENT AND MAGNITUDE-BASED SYSTEM IDENTIFICATION OF TORNADO-ASSOCIATED INFRASOUND

Major Field: Aerospace Engineering

Biographical:

Education:

Received a Bachelors of Science in Aerospace Engineering with honors at Oklahoma State University in May 2019.

Received a Bachelors of Science in Mechanical Engineering at Oklahoma State University in May 2019.

Experience:

John Brammer Graduate Research Fellow

Glenn and Mary Lou Penisten Graduate Fellow

Research Assistant at Oklahoma State University

Professional Affiliations:

AIAA Student Member

APS Graduate Student Member

ASA Student Member